





Review

Nanostructured Anodic Copper Oxides as Catalysts in Electrochemical and Photoelectrochemical Reactions

Damian Giziński ^{1,*}, Anna Brudzisz ¹, Janaina S. Santos ², Francisco Trivinho-Strixino ²,
Wojciech J. Stępniewski ^{1,*} and Tomasz Czujko ^{1,*}

¹ Institute of Materials Science and Engineering, Faculty of Advanced Technology and Chemistry, Military University of Technology, 2 Kaliskiego Str, 00908 Warsaw, Poland; anna.brudzisz@wat.edu.pl

² Department of Physics, Chemistry and Mathematics, Federal University of São Carlos (UFSCar), Via João Leme dos Santos Km 110, Sorocaba 18052-780, Brazil; janasoares@ymail.com (J.S.S.); fstrixino@ufscar.br (F.T.-S.)

* Correspondence: damian.gizinski@wat.edu.pl (D.G.); wojciech.stepniewski@wat.edu.pl (W.J.S.); tomasz.czujko@wat.edu.pl (T.C.); Tel.: +48-261-83-94-45 (T.C.)

Received: 28 October 2020; Accepted: 13 November 2020; Published: 17 November 2020



Abstract: Recently, nanostructured copper oxides formed via anodizing have been intensively researched due to their potential catalytic applications in emerging issues. The anodic Cu₂O and CuO nanowires or nanoneedles are attractive photo- and electrocatalysts since they show wide array of desired electronic and morphological features, such as highly-developed surface area. In CO₂ electrochemical reduction reaction (CO₂RR) copper and copper-based nanostructures indicate unique adsorption properties to crucial reaction intermediates. Furthermore, anodized copper-based materials enable formation of C₂₊ hydrocarbons and alcohols with enhanced selectivity. Moreover, anodic copper oxides provide outstanding turnover frequencies in electrochemical methanol oxidation at lowered overpotentials. Therefore, they can be considered as precious metals electrodes substituents in direct methanol fuel cells. Additionally, due to the presence of Cu(III)/Cu(II) redox couple, these materials find application as electrodes for non-enzymatic glucose sensors. In photoelectrochemistry, Cu₂O-CuO heterostructures of anodic copper oxides with highly-developed surface area are attractive for water splitting. All the above-mentioned aspects of anodic copper oxides derived catalysts with state-of-the-art background have been reviewed within this paper.

Keywords: carbon dioxide reduction reaction; anodic copper oxides; nanostructures; photoelectrochemical water splitting; direct methanol fuel cells; photodegradation; renewable energy; greenhouse gases; glucose sensors

1. Introduction

Anodic oxides are well-known for their applications in metals corrosion protection. Compact, adherent and hard oxide coatings prevent majority of aluminum alloys items and devices from the degradation [1–3]. This approach is widely applied in industry—for example: bodywork of aircrafts, aluminum alloys turbine blades, and smartphones are anodized.

A certain milestone in the field of anodizing has been reported by Masuda and Fukuda in 1995 [4]. It had been noticed earlier that the anodic oxide on aluminum is nanoporous [5], however Masuda and Fukuda have experimentally proven that the arrangement of the nanopores can be significantly improved. They have reported a two-step anodizing that leads to the formation of hexagonally arranged, honey-comb like nanostructures [4]. Since this breakthrough, tremendous progress in anodic alumina template-assisted nanofabrication of nanowires, nanotubes and nanodots has taken place [6].

Achievements in nanostructuring of alumina via anodizing encouraged scientists world-wide to research anodizing of other metals. Many metals have been anodized, leading to the progresses in: superhydrophobic and superhydrophilic surfaces (mainly Al [7–9]), nanofabrication (mainly Al [6,10–12]), improved performance of biomaterials (mainly Al [13,14] Ti [15]), drug releasing platforms (mainly Ti [16,17]), lab-on-chips (mainly Al [18]), optical and electrochemical sensors (mainly photonic crystals made on Al [19–21], and nanostructures formed via anodic alumina template-assisted nanofabrication [22]), photonic and luminescent materials (mainly Al [19–21] and Ti [23]), heat transport (mainly nanostructures formed using anodic Al₂O₃ [12] and anodic alumina itself [24,25]), photocatalytic and photoelectrochemical reactions (i.e., Al [11], Ti [26–28], Fe [28], Zr [28,29], Cu [30,31] and W [32,33]), surface enhanced Raman spectroscopy (i.e., Zr [34], Ti [35], Al [36]), dye sensitized solar cells (mainly Ti [37,38]) and structural color generation (mainly Al [19–21,39,40]).

The majority of the anodic oxides have a few common features:

- Fixed stoichiometry (despite some minor fluctuations of the composition associated with the anions incorporation);
- Amorphous crystal structure, however, in particular cases, anodic ZrO₂ [41,42], and FeAl₂O₄ [43,44] were reported to be crystalline (when as-anodized samples were examined);
- Consist of nanopores or nanotubes (except ZnO which is made of nanorods [45]).

Therefore, anodic oxides grown on copper seem to be unique due to the following features:

- Have developed surface area due to their morphology, i.e., nanowires, nanoneedles or nanorods [46];
- Their stoichiometry is not fixed: Cu₂O, CuO, and Cu(OH)₂ co-exist in as-obtained samples [46];
- In as-anodized samples crystalline phases: cuprite (Cu₂O) and tenorite (CuO) are present [46].

Therefore, these unique features, combined with high surface area, make copper anodizing interesting for both: fundamental research and their applications, especially in catalysis, due to the developed surface area and properties of Cu₂O and CuO.

2. Anodic Copper Oxides—Unique Features and Applications

2.1. Morphology and Composition of Nanostructures Grown by Copper Anodizing

In electrochemical fabrication of the nanostructured copper oxides, two major approaches can be distinguished [46]:

- Passivation of copper using potentiostat/galvanostat;
- Anodization of copper employing standard 2-electrode system.

Using potentiostat one can easily find an optimal electrolyte for a given system (from Pourbaix diagram) [47] and determine appropriate potential range from polarization experiment (passivity range) [48]. On the other hand, two-electrode approach allows to scale-up easily anodizing procedure and is much more promising for large scale applications.

The potentiostat-based approach allows formation of: nanoneedles (1.0 M NaOH, –200 mV vs. Ag|AgCl—see Figure 1a [49], 1.0 M KOH, –200 mV vs. Ag|AgCl, RT, 1 h [50], 0.5–4.0 M KOH, 0.5–4.0 mA cm^{–2}, 5–25 °C, 5–40 min [51], 0.5 M KOH, Linear Stripping Voltammetry (LSV) at scan rate ranging from 10 mV s^{–1} to 30 mV s^{–1} [52], 2.0 M KOH, 1.5 mA cm^{–2} [53], 2.0–3.5 M KOH, 1.5 mA cm^{–2} at temperature up to 28 °C [54]), nanotubes (2.5 M KOH, 1.5 mA cm^{–2} at temperature up to 28 °C [54]), nanoparticles (3.5 M KOH, 1.5 mA cm^{–2} at 28 °C [54]) and dendrite crystals (1.0 M NaOH, linear scan with 40 mV s^{–1} rate since –1.6 V up to 0.4 V vs. SCE [55]). Using potentiostat, we have also recently explored passivation regimes in electrolytes with lower pH, like 0.1 M NH₄HCO₃ (Figure 1b; unpublished research).

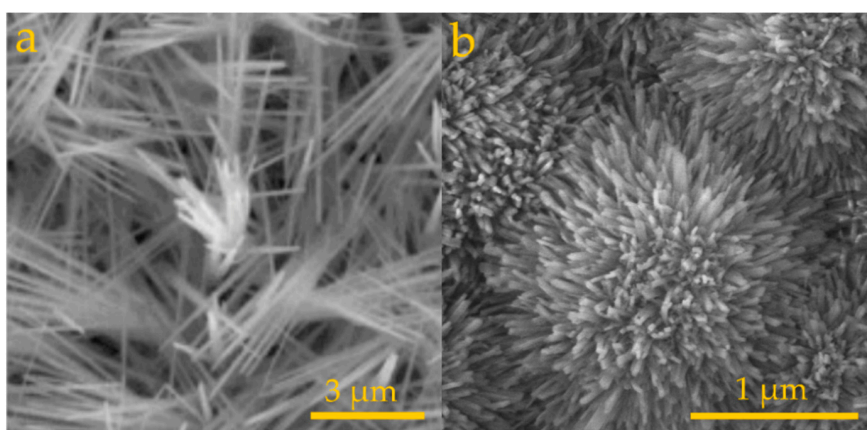


Figure 1. FE-SEM images of nanostructured oxides formed by copper passivation in 1.0 M NaOH (a) (−200 mV vs. Ag|AgCl, 10 min) [49] and 0.1 M NH_4HCO_3 (b) (−200 mV vs. Ag|AgCl, 14 h; unpublished results by A. Brudzisz, D Giziński, W.J. Stępniewski et al.). (a) has been reproduced from [49] © 2019 Elsevier.

Much greater diversity of morphology is reported when a standard, two-electrode system is applied for copper anodizing. For example, Allam and Grimes [56] reported in their study, formation of cross-linked needle/ribbon nanoarchitectures (solution of KOH at pH = 11, 10 V), dendrites (0.2 M KOH + 0.1 M NH_4Cl , 6 V, 300 s), nanopores (0.15 M KOH + 0.1 M NH_4F , 6 V, 300 s), and leaf-like structures (0.15 M KOH + 0.1 M NH_4F + 3% H_2O in ethylene glycol, 30 V, 300 s). Copper anodizing in NaOH in two-electrode system allows formation of nanoneedles (1.0 M NaOH, 6 mA cm^{-2} , 5 min, 25 °C) [57]. Moreover, what is in-line in Allam and Grimes findings [56], modification of the anodizing electrolyte has a significant impact on the oxides' morphology: addition of chlorides allows formation of chrysanthemum-like nanostructures (4 g L^{-1} NaOH + 1200 g L^{-1} NaCl, 0.2 mA cm^{-2}) [58], while anodization in ethylene glycol (EG) based, fluoride rich electrolyte allows formation of nanoporous oxide (EG based electrolytes containing: 0.1–0.5 M KOH, 1 vol% H_2O , up to 0.1 wt% NH_4F ; 20 V, 5 °C, 15 min) [59].

In the case of copper, there are still numerous unexplored regimes of anodizing that lead to new nanostructures formation. Recently, copper anodizing in aqueous solution of salts with alkaline hydrolysis, namely in 0.1 M Na_2CO_3 (Figure 2a–c; 3–31 V, 1 h, 20 °C [60]) and 0.1 M K_2CO_3 (Figure 2d–f; 5–50 V, 1 h, 10 °C [61]) allowed formation of nanorods and nanowires, respectively.

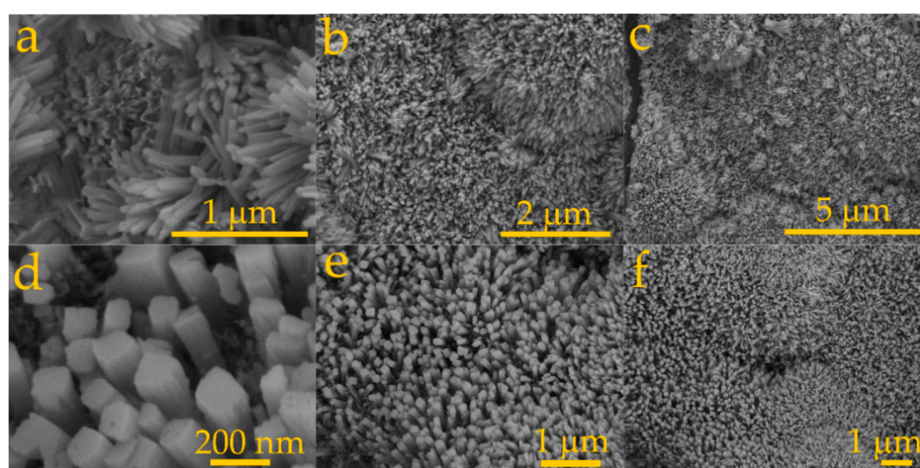


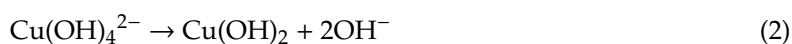
Figure 2. FE-SEM images of nanostructured oxides formed by copper anodizing in 0.1 M Na_2CO_3 (a–c) (31 V, 1 h, 20 °C) [60] and 0.1 M K_2CO_3 (d–f) (35 V, 1 h, 10 °C [61]). (a–c) has been reproduced from [60] © 2020 Elsevier. (a,d–f) has been reproduced from [61] © 2019 Elsevier.

The varied morphologies with detailed experimental procedures have been collated in review paper [46] and book chapter [62].

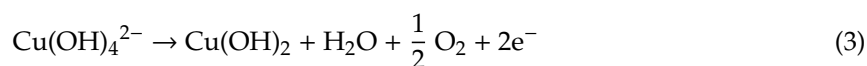
Variety of the morphologies of the anodic nanostructures formed on copper results from much more complex mechanism of growth, when compared to the other nanostructured anodic oxides. It is generally accepted that the nanostructured anodic oxides grow as an effect of two driving forces: oxidation of metal, forming passive/anodic layer and field-assisted etching. In the case of copper, re-deposition of Cu^{2+} species is also involved [63]. Namely, during copper passivation/anodizing in alkaline media, water soluble copper species like $\text{Cu}(\text{OH})_4^{2-}$ are formed as an effect of metallic copper oxidation and alkaline environment [52]. However, during anodizing, there is a local pH drop on the surface of the anode, caused by oxidation of hydroxyl anions (1):



It means that locally, at the anode, above mentioned water soluble species precipitate, forming $\text{Cu}(\text{OH})_2$, according to the pH shift (2):

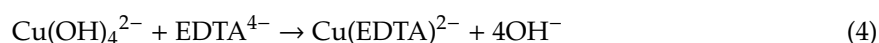


Overall, phenomena at the anode can be considered according to the following reaction (3):



It means, that re-deposited copper (II) hydroxide precipitates, and subsequently participates in the formation of the nanostructures. Of course, $\text{Cu}(\text{OH})_2$ can decompose into CuO and H_2O , increasing the amount of the obtained cupric oxide. This phenomenon makes formation of anodic copper oxides unique, from the mechanistic point of view.

What is interesting, when the redeposition is blocked, totally different morphology of the formed materials is obtained [63]. For example, when ethylenediaminetetraacetic acid (EDTA) is added into the electrolyte, re-deposition of copper is halted due to the chelate effect (4) [63]:



and different morphology of the anodizing product is obtained. For example, when copper is anodized in 0.01 M KHCO_3 nanorods are formed in wide range of applied voltage [63]. When anodizing is performed in an electrolyte containing 0.01 M KHCO_3 and 10^{-3} M EDTA, nanoparticles are formed and in an extreme situation, when electrolyte composed of 0.01 M KHCO_3 and 0.01 M EDTA at 10 V nanopores are formed. Therefore, for the same base electrolyte and same voltage, depending on the concentration of EDTA, as redeposition hindering agent, various morphologies are obtained. What is even more interesting and in line with the assumptions, the more the EDTA in the electrolyte the less CuO is present in the formed oxide layer (confirmed by Raman Spectroscopy) when compared to Cu_2O and the less crystalline tenorite (CuO) when compared to cuprite (Cu_2O) (confirmed by X-ray Diffraction) [63]. It means that redeposition during copper anodizing is also a supplementary source of the Cu^{2+} species in the anodically formed nanostructures.

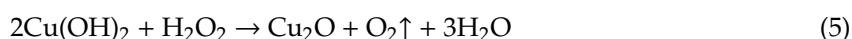
X-ray Photoelectron Spectroscopy (XPS) studies clearly reveal that the nanostructures formed by anodic oxidation of copper consist of Cu_2O , CuO , and sometimes $\text{Cu}(\text{OH})_2$ which was repeatedly confirmed by deconvolution of binding energies peaks for $\text{Cu}2\text{p}_{3/2}$, $\text{Cu}2\text{p}_{1/2}$, and $\text{O}1\text{s}$ orbitals [62]. Carbonates [60] and fluorides [59] from the electrolytes were also found to be incorporated into the anodically grown nanostructures. This is analogous to the anions incorporation into anodic aluminum oxide [64,65]. Furthermore, X-ray diffraction (XRD) experiments reveal that the formed nanostructures are made of two major crystal phases: monoclinic tenorite (CuO) and cubic cuprite (Cu_2O) [62].

Simultaneously, for results where XPS show presence of $\text{Cu}(\text{OH})_2$ no reflections from crystalline $\text{Cu}(\text{OH})_2$ is found that means that the formed $\text{Cu}(\text{OH})_2$ is amorphous.

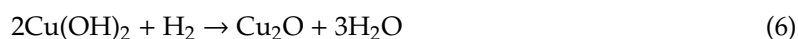
Nevertheless, composition of the nanostructures formed by copper anodizing can be tuned. For certain applications, materials composed of only Cu_2O or CuO are demanded. Moreover, in many cases crystallinity of the nanostructures is a highly desired feature. The simplest way to achieve crystallinity of as-obtained nanostructures is post-annealing. It leads to thermal decomposition of $\text{Cu}(\text{OH})_2$ into CuO and H_2O that evaporates (temperature range 250–400 °C is usually applied for this purpose) and crystallization of tenorite and cuprite, which is confirmed by intensity increase of corresponding reflections in XRD patterns [62,66,67]. When the annealing was conducted in the furnace under air atmosphere, oxidation of Cu_2O into CuO also occurred [62,66].

Another way to increase the oxidation state of copper in the nanostructured anodic oxides is chemical oxidation. Arurault et al. reported that immersion of as-anodized samples in a solution containing 3 wt% of NaOH and 3 wt% KMnO_4 (4 min at 50 °C, followed by drying at 90 °C for 15 min) allowed to obtain surface coating composed mainly of CuO with traces of Cu_3O_2 [68].

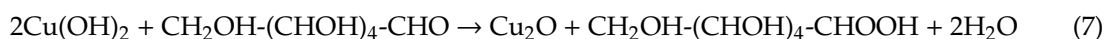
On the other hand, reduction of $\text{Cu}(\text{II})$ to $\text{Cu}(\text{I})$ on anodic copper oxides was also studied. Zhang et al. [30] reported three various routes for anodic copper oxides chemical reduction into Cu_2O . One of them is reduction of Cu^{2+} species via decomposition of hydrogen peroxide (5):



Annealing of as-obtained anodic copper oxides in hydrogen atmosphere at 280 °C also results in Cu^{2+} species reduction (6):



Another, much more facile method is reduction of copper (II) hydroxide by glucose (7):



Therefore, anodization and passivation of copper result in variety of morphologies. Moreover, their post-synthesis treatment enables formation of nanostructures with desired chemical composition, tailored for certain applications.

2.2. Applications of Electrochemically Grown Copper Oxides

One of the most conventional applications of anodic oxides is corrosion protection. Despite the fact that copper is a semi-noble metal, it still may undergo corrosion—especially crevice and pitting corrosion might be dangerous for this metal. Mahmood et al. reported formation of oxide “grain” on copper (diameter ranging from 25 to 68 nm) that slowed down corrosion in both neutral and alkaline environment [69]. In 3.5% NaCl aqueous solution corrosion rate decreased from 0.083 mm y^{-1} (copper without surface treatment) to 0.011 mm y^{-1} after anodizing. When $2 \text{ mg L}^{-1} \text{ NH}_3$ solution was applied as the electrolyte, the corrosion rate after anodizing was as small as 0.070 mmy^{-1} . More sophisticated approach has been reported by Xiao et al. [51]. In their research, anodizing of copper resulted in the formation of oxide nanoneedles. Since nanoneedles can be strongly defected (oxygen vacancies provide polarity of the surface), they were coated with FAS-17 (2H,2H-perfluorodecyltriethoxysilane). After the coating, a lotus-leaf effect was observed—the treated surface gained hydrophobicity and the wetting contact angle was equal 169° . As prepared hydrophobic surfaces were examined for corrosion protection—polarization curves were approximated using Tafel’s equation and charge transfer resistance was obtained via Electrochemical Impedance Spectroscopy (EIS). The conducted research revealed that after 1 day of immersion in 3.5% NaCl the anodized and FAS-17 coated samples have corrosion potential as small as $-124 \text{ mV vs. Ag|AgCl|3 M KCl}$, while as-anodized samples had corrosion potential equal $-121 \text{ mV vs. Ag|AgCl|3 M KCl}$ (not-treated reference sample had corrosion potential equal $-254 \text{ mV vs. Ag|AgCl|3 M KCl}$). What is more impressive, corrosion current density analysis showed

that the treatment significantly slowed down the corrosion rate. Namely, anodized and FAS-17-coated samples had corrosion current density as low as $0.66 \mu\text{A cm}^{-2}$ (what translates in corrosion rate equal 0.016 mm y^{-1}). Simultaneously, not treated and as-anodized samples current densities were equal 19.58 and $9.11 \mu\text{A cm}^{-2}$, respectively (corrosion rate decreases from 0.44 to 0.21 mm y^{-1} , respectively). Furthermore, EIS-derived charge transfer resistance (R_{CT}) increased from 0.25 (not treated samples) to 2.47 k Ω (anodized and FAS-17 coated samples) vs. 0.44 k Ω for only anodized sample. The data show a synergistic effect of anodic coating protection and superhydrophobicity of the surface. The worse the contact between the electrolyte and the protected metal surface, the better the corrosion protection. Data acquired for samples immersed for 1 week in 3.5% NaCl revealed that the excellent performance of anodized and FAS-17 coated samples was maintained: corrosion potential equaled -134 mV vs. Ag|AgCl|3 M KCl, corrosion current density and corrosion rate equaled $0.99 \mu\text{A cm}^{-2}$ and 0.023 mm y^{-1} respectively, while R_{CT} was equal 1.91 k Ω . It translates into still much better corrosion performance than for only-anodized samples (note that corrosion potential of only-anodized and anodized and FAS-17 coated samples were comparable and both were much more noble than for not-treated, reference sample).

Similar surface treatment procedure, anodizing and FAS-17 bonding, was applied by Jiang et al. in order to hinder scale formation on copper [57]. Generally, due to its great thermal conductivity, copper is frequently used in heat exchange devices. In such systems, tap water is commonly applied as a cooling medium. Tap water contains Mg^{2+} and Ca^{2+} cations that precipitate as MgCO_3 and CaCO_3 , forming scale that worsens performance of the device. The effect of copper anodizing and coating with FAS-17 on scale formation was researched using CaCO_3 . It was shown that the greater the contact angle (increased from 4.5 to 154° for water and from 0 to 133° for CH_2I_2 after anodizing and FAS-17 coating) the less CaCO_3 crystallizes on the surface. The results reveal that, the surface functionalization can extend performance of a heat-exchanging device without a failure.

Another application arising from the surface morphology of anodically grown nanostructures on copper is formation of pH-switchable meshes [53]. What is very important, research reported in this paper shows that even very developed surface area of substrate leads to formation of uniform nanostructures. Anodizing in 2.0 M KOH allowed formation of high-aspect ratio nanoneedles. Afterwards, the nanoneedles were coated with gold via sputtering and then material was immersed for approx. 12 h in 1 mM ethanol solution of thiols, containing $\text{HS}(\text{CH}_2)_9\text{CH}_3$ and $\text{HS}(\text{CH}_2)_{10}\text{COOH}$, what allowed chemical bonding of the compounds to the formed nanostructures. The permeation of the mesh was strictly related to the pH of the applied solution: at pH = 12 or greater, the contact angle was equal 8° and the mesh was permeable. In contrary, at lower pH, the contact angle equals 153° and the mesh is not permeable for water anymore. What is the most interesting, the response-time of the mesh is 3 s. Thus, it can be considered as a real-time pH-responsive surface.

Another application of nanostructures formed via electrochemical copper oxidation was reported by Ratyński et al. [70]. Authors anodized copper in 2.5 M NaOH at 3.0 mA cm^{-2} and subsequently annealed it at 80°C . Obtained nanostructures served as cathodes in batteries, showing that CuO_x nanostructures can easily compete with currently available technologies. Namely, the practical energy density for anodized copper oxide based cell equals 192 Wh kg^{-1} (mass includes current collector) versus 150 Wh kg^{-1} reported for alkaline zinc-manganese oxides and $155\text{--}230 \text{ Wh kg}^{-1}$ for Li-MnO₂ spirally wound cell. Self-discharge ("shelf-life") of the anodic CuO_x base cells is also relatively low, what is also crucial in energy storage: after 30 days of storage only $0.7 \pm 0.5\%$ of energy of the cells was lost. Wang et al. used similar procedure for batteries electrode formation [71]. In their experiment, after anodizing in 1.0 M KOH at 10 mA cm^{-2} for 10 min, the samples were also annealed at 185°C for 1.5 h in order to convert all $\text{Cu}(\text{OH})_2$ into CuO . Authors used porous copper foam (macro-porous framework) as a starting material for anodizing and as an effect a 3D morphology with extremely developed surface area was obtained. It was found to be beneficial for the electrode performance. Authors have shown that after 100 charge-discharge cycles the Coloumbic efficiency of the cells remained at 50% for CuO_x 3D morphology obtained by foam anodizing while

for anodized copper foil it dropped to ca. 13%. Moreover, when compared to other copper-based cells, anodization of copper foam appears to be the most promising approach for energy storage applications: comparison to other techniques shows that for the reported approach material capacity after 100 charge-discharge cycles remained at the level of 510 mA g^{-1} , for nanospheres it reached 500 mA g^{-1} (after 40 cycles), and found to be as low as 91 mA g^{-1} for hollow nanospheres after 50 cycles. Therefore, formation of CuO_x via anodizing is beneficial due to its composition (high practical energy density, long shelf-life [70]) and morphology (anodization of Cu-foam [71]) for energy storage applications and has large commercialization potential.

Qin et al. reported research in which $\text{Cu}_{40}\text{Zr}_{50}\text{Ag}_{10}$ metallic glass obtained by spin melting was firstly dealloyed in HF (in order to remove Zr) and subsequently anodized (0.5 M KOH, 10 mA cm^{-2} , 5–7 min) and calcinated ($200 \text{ }^\circ\text{C}$, 2 h) [72]. Formed nanowires (25–35 nm in diameter) were composed of CuO_x decorated with Ag nanoparticles (12–13 nm in diameter). Furthermore, the impact of the fabricated nanostructures on bacterial cells culturing was investigated: after 12 h of *E. coli* incubation 3–4 colonies were found (depending on anodizing time), while for the blank control sample, 311 bacterial colonies were found to be present. The antibacterial performance of the material is attributed mainly to the presence of Ag nanoparticles.

Arurault et al. reported formation of anodic oxide layer on copper via anodizing in an electrolyte containing 10 wt% NaOH and 5 wt% NaClO_2 (60° , 15 min) [68]. The anodizing was followed by chemical oxidation in a mixture containing 3 wt% NaOH and 3 wt% KMnO_4 ($50 \text{ }^\circ\text{C}$ for 4 min followed by drying at $90 \text{ }^\circ\text{C}$ for 15 min). As previously mentioned, due to the chemical oxidation, except CuO, metastable Cu_3O_2 was also found in the formed oxide coating, as formed black coatings served as light absorbers [68]. Typically, light absorbers with satisfactory properties (i.e., absorptivity at the level of $\alpha = 0.94$, emissivity at the level of $\varepsilon = 0.14$) used to be based on hazardous chemicals, including Cr(VI) species and were not stable above $200 \text{ }^\circ\text{C}$. Approach based on copper anodizing allowed to form absorptive, black coatings on copper without use of environmentally hazardous chromates. Additionally, the satisfactory performance of the film was maintained even above $200 \text{ }^\circ\text{C}$: at $220 \text{ }^\circ\text{C}$ in both vacuum and under air atmosphere, the absorptivity was as high as $\alpha = 0.96$.

To sum up, on the one hand, anodic copper oxides nanoneedles and nanowires were found to be beneficial in applications, where highly developed surface area is demanded. On the other hand, chemical composition enables opportunities in application of the anodic copper oxides where properties of CuO and Cu_2O might bring contribution. What is worth noting, CuO and Cu_2O are semiconductors with band gap ranging from 1.2 to 2.16 eV (*p*-type semiconductor) and 2.1 to 3.8 eV respectively [73,74]. It means that both compounds have band gaps in the visible light range and are attractive for photocatalytic applications.

Therefore, highly-developed surface area, attributed to the nanostructured morphology and properties of anodic copper oxides, resulting from chemical composition, prerequisite the anodic copper oxides for applications in catalysis, especially when they can contribute in emerging issues, like renewable energy harvesting and greenhouse gases reduction. The major goal of this review is state-of-the-art literature analysis focusing on nanostructured anodic copper oxides application in electrochemical and photoelectrochemical reactions, exploring potential solutions nowadays to such issues like carbon dioxide reduction reaction or photoelectrochemical water splitting.

3. Electrochemical CO_2 Reduction Reaction

Since the preindustrial age, humanity has been constantly affecting natural environment by releasing enormous amount of CO_2 to atmosphere. Concentration of this greenhouse gas has doubled since the 1800s, mainly due to the fact that combustion of fossil fuels has been our main energy source [75,76]. Increased accumulation of atmospheric CO_2 is a major anthropogenic origin of today's global warming [77]. In order to hinder the climate change and maintain relatively sustainable temperature increase, net CO_2 emission needs to be decreased to zero by 2050 [78]. Beside limiting fossil fuels usage, this goal can be achieved by recycling of the CO_2 that is being released in i.e., coal,

petrol, and natural gas incineration. In this light, carbon cycle could be closed by CO₂ reversion into value-added fuels and chemicals. This approach would enable sustainable energy recovery and inhibit progressive trend of climate change.

One of the prominent strategies for transforming this greenhouse gas into value-added products is CO₂ electroreduction reaction (CO₂RR). Carbon atom in CO₂ is at its highest oxidation state which needs to be reduced by electrons intake in order to convert this molecule into more energetic form. To overcome thermodynamic limitations associated with the process, CO₂ reduction is conducted in electrocatalytic cell, where cathode act as electrocatalyst for CO₂RR. Hence, in such a configuration, cathodic CO₂ reduction (8) competes with hydrogen evolution reaction (HER) (9).



Electrons and protons consumed in the cathodic process are produced in oxygen evolution reaction (OER) that proceeds on anode (10):



Nonetheless, mechanism of electrochemical CO₂RR is a complicated matter since CO₂ hydrogenation occurs via multiple steps yielding variety of possible products. Additionally, mechanism and possible reaction pathways of CO₂RR are highly dependent on catalyst specification and reaction conditions, such as electrolyte, pH and applied potential. CO₂ molecule can be converted into CO, hydrocarbons and oxygenates through reduction by intaking two, four, six, or even eighteen electrons when reaction leads to propanol formation (Table 1). However, independently of the final outcome, first step of the reaction relies on one electron CO₂ activation which results in formation of unstable CO₂⁻ radical [79]. Activated molecule may adsorb on catalyst surface, undergo protonation or react with other species or reaction intermediates. In heterogenous catalysis, surface process occurs via three main steps: substrates adsorption, surface reaction and products desorption. During CO₂RR to C₁ compounds, activated CO₂ molecule adsorbed on catalyst surface undergoes transformation into *CO (C-O cleavage) followed by protonation to form C-H bonds and eventual desorption after atoms rearrangement. When reaction yields C₂₊ products CO₂RR mechanism becomes more complicated due to additional C-C bond formation associated with increased number of electrons and protons taking part in the conversion of CO₂. Reaction pathway through carbon-carbon coupling is a debatable topic and various mechanistic explanations were reported, such as C-C formation via *CO dimerization [80] and protonated *CHOCO intermediate [81].

Table 1. Selected pathways of CO₂ reduction with equilibrium potentials.

Possible CO ₂ Reduction Reactions	E ₀ [V vs. RHE]
CO ₂ + 2H ⁺ + 2e ⁻ → HCOOH _(aq)	-0.12
CO ₂ + 4H ⁺ + 4e ⁻ → C _(s) + 2H ₂ O	0.21
CO ₂ + 6H ⁺ + 6e ⁻ → CH ₃ OH _(aq) + H ₂ O	0.03
CO ₂ + 8H ⁺ + 8e ⁻ → CH _{4(g)} + 2H ₂ O	0.17
2CO ₂ + 10H ⁺ + 10e ⁻ → CH ₃ CHO _(aq) + 3H ₂ O	0.06
2CO ₂ + 12H ⁺ + 12e ⁻ → C ₂ H _{4(g)} + 4H ₂ O	0.08
2CO ₂ + 14H ⁺ + 14e ⁻ → C ₂ H _{6(g)} + 4H ₂ O	0.14
3CO ₂ + 16H ⁺ + 16e ⁻ → C ₂ H ₅ CHO _(aq) + 5H ₂ O	0.09
3 CO ₂ + 18H ⁺ + 18e ⁻ → C ₃ H ₇ HO _(aq) + 5H ₂ O	0.10

The only pure metal that enables C₂₊ products formation in CO₂RR is copper. In 1985, Hori et al. [82] reported their pioneering work on product distribution of constant-current CO₂

electrolysis with various polycrystalline metal electrodes. This initiated a series of experimental investigations performed to unveil selectivity of pure metal electrodes in electrochemical CO₂RR [83,84].

According to those findings, tested metals can be divided into four groups on the basis of their affinity to different products during 1 h CO₂RR in 0.5 M KHCO₃ electrolyte and at constant current density (geometric) of -25.0 mA cm^{-2} . The first group of metals converts CO₂ mainly into formate (i.e., Pb, In, Sn), the second produces mainly CO (i.e., Pd, Au, Ag) and the third favors HER (i.e., Ni, Fe and Pt). Finally, copper was featured as a separate class due to its unique ability to produce C₂₊ hydrocarbons and alcohols in conducted tests. Various selectivity of transition metals to reduce CO₂ results from differences in their binding energy to crucial intermediates of CO₂RR and HER, such as *CO and *H (Figure 3).

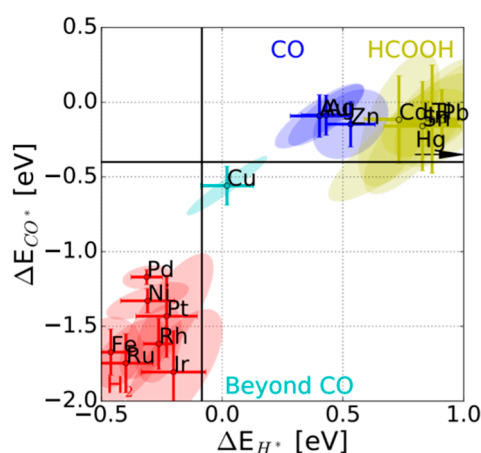


Figure 3. Categorization of transition metals based on their binding energies to *CO and *H. Reproduced from [85] © 2017 Wiley-VCH.

The unique properties of copper may be explained by the fact that it is the only pure metal that indicates moderately negative adsorption energy for *CO and slightly positive adsorption energy for *H. Therefore, copper surface favors adsorption of *CO leading to higher probability of CO₂RR over HER. Additionally, Cu moderate adsorption energy for *CO appears to be sufficient to enable its activation for further reduction and subsequently support C-C coupling (Sabatier principle) [86,87]. Other transition metals bind *CO whether too strongly or too weakly to activate the molecule for further transformation towards C₂₊ products. Considering exceptional properties of copper in electrocatalytic CO₂ reduction, development of new Cu-based catalyst seems to be a promising strategy to turn excessively emitted CO₂ into liquid fuels and feedstock chemicals.

Despite those exceptional properties of copper in reducing CO₂, catalysts based on this metal can be further modified in order to improve its catalytic performance in CO₂RR. Copper electrodes that are derived from oxidized metal are an example of such optimization. Family of oxide-derived copper (OD-Cu) catalysts is gaining more and more attention since it shows significantly higher affinity towards C₂₊ products when compared to bare copper [88]. OD-Cu materials are made in two steps: (i) copper oxidation performed prior to the electrocatalytic reaction and (ii) subsequent reduction of oxidized surface layer during CO₂RR. Oxidation phase leads to formation of nanostructured oxide layer on copper surface which is reconverted into metallic form when inserted to reducing CO₂RR media, leaving highly roughened copper surface. This redox cycle introduces numerous changes to catalyst morphology enhancing copper catalytic ability to selectively transform CO₂ into C₂₊ products [89,90]. One of the most expected results obtained from the surface roughening via redox treatment is expansion of geometric, and consequently, electrochemically active surface area (ECSA). Oxidation of CO₂RR intended copper electrodes yields various types of nanostructures depending on method, process conditions and oxidizing agents. As it was reported, nanowires (NW) [91,92], nanoneedles (NN) [93], nanocrystals (NC) [94,95], and nanoparticles (NP) [96,97] of copper oxides and/or hydroxides can be

produced during OD-Cu catalyst preparation. Gao et al. [98] reported ECSA of O₂-plasma oxidized Cu that was 44 times larger than parent Cu flat foil after 1 h of CO₂RR. Roughened material with high ECSA showed enhanced catalytic performance in the investigated system. However, in spite of intuitive implication that higher ECSA of rough OD-Cu leads to better reactivity, surface area and catalytic efficiency correlation requires deeper consideration [99]. In a consecutive oxidation/reduction processes, development of large surface area increases number of surface defects that can act as the active sites governing electrocatalytic surface reaction. Furthermore, active sites generated during redox OD-Cu synthesis are highly diverse and represent defects with different coordination. This lack of active sites' homogeneity mirrors their different catalytic potential and ability to support given surface reaction [100]. Therefore, while discussing surface-activity dependence in OD-Cu catalyzed CO₂RR, both quantitative and qualitative analyses need to be performed.

The nature of copper active sites generated via surface modification in OD-Cu synthesis alters adsorption energies for CO₂RR intermediates and consequently material selectivity. In general, active sites that indicate strong binding interaction with *CO favors C₂ products formation, whereas weakly adsorbed CO groups are more likely to be converted into C₁ product. Verdaguer-Casadevall et al. [101] investigated binding energies of CO on OD-Cu versus polycrystalline Cu. It was proposed that grain boundaries of OD surface show strong Cu-CO binding interactions and are the main active sites that facilitate C-C formation. Therefore, application of OD-Cu catalysts with grain boundaries-rich surfaces could accelerate CO dimerization, a rate-limiting step of CO₂ to C₂ conversion [80]. Another study [102] shows various catalytic performance of different Cu₂O facets and their separating boundaries/interfaces in OD-Cu catalyst. As reported, there was a synergistic effect in catalyst that possesses mixed (111) and (100) Cu₂O. In this case, (100) facet was found to support C₂H₄ formation with 45% FE and (111) with 38% FE due to the difference in CO binding energy. Stronger interactions between CO and (100) was a reason for higher ethylene production. However, as provided by theoretical calculations, combined effect of both facets in OD-Cu increased FE for ethylene up to 59%. It was reasoned by the fact that facets boundaries are additional strong binding sites enhancing C-C formation (together with (100) facet), whereas neighboring (111) facet displayed weak Cu-C₂H₄ binding facilitating C₂ product desorption. This finding was confirmed in literature [103] which also highlights facets effect on Cu catalyzed CO₂RR. It was stated that Cu (100) supports C₂ formation, Cu (111) favors C₁ products, and Cu (110) enables generation of C₂ and C₃ oxygenates.

Another important feature introduced to OD-Cu based materials by redox modification is incorporation of different copper valences to catalyst surface. In their comparative studies, Xiao et al. [104] assumed three simulated models representing pure Cu (111) facet, pure Cu₂O (111) and Cu embedded in oxidized matrix as CO₂RR catalysts to study the influence of Cu⁺ on the process. As reported, mixed valences (Cu⁰/Cu⁺) catalyst displayed the lowest energy barrier (0.27 eV) for CO₂ physisorption as an initial, CO₂ activating phase of the reaction. On pure Cu⁰ and Cu⁺ surfaces the value was significantly higher and reached 0.49 eV and 0.56 eV, respectively. Superior CO₂ physisorption on Cu⁰/Cu⁺ was explained by the additional stabilization of *CO₂ species by water molecules adsorbed at Cu⁺ sites. Moreover, surface composed solely of Cu⁺ was found unstable during CO₂RR leading to formation of C₁ oxygenates which denies the statement that oxidized copper itself is behind great C₂₊ selectivity of OD-Cu. A similar conclusion was found for CO dimerization on modelled systems. Cu embedded Cu₂O matrix showed the lowest energy barrier for this C₂ formation rate-limiting step [105]. Carbon atoms in CO species adsorbed at Cu⁰ and Cu⁺ carry opposite charges, which facilitates their dimerization by mutual attracting interactions. This phenomenon decreased energy barrier for the process to 0.71 eV for mixed valence surface from 1.10 eV and 3.15 eV for pure metal and oxide phases, respectively. Furthermore, CO dimerization was found to be less energy demanding than CO protonation (C₁ product formation mechanism) on Cu⁰/Cu⁺. Enhanced ability of Cu⁺ containing Cu catalysts to selectively convert CO₂ into C₂₊ products was proven by many experimental research reports [106,107].

Besides strictly morphological aspects of OD-Cu catalysts, surface roughening achieved by oxidation-reduction cycle impacts CO₂RR catalytic system by tuning the pH value near catalyst surface. The local pH effect over OD-Cu relies on higher consumption of protons due to remarkably larger surface area leading to increased concentration of OH⁻ ions near roughened surface [108,109]. Well-developed surface area of modified catalysts increases initial efficiency of protonation processes: HER and CO₂RR which generates pH gradient from solid-liquid interface to bulk. It was reported that pH values of CO₂ saturated 0.1 M KHCO₃ over OD-Cu can differ from 6.8 in bulk solution to 9.8 near to the surface (−1.8 V vs. SCE) [110] and from 6.8 to 10.8, respectively, as showed by theoretical studies [111]. Those changes in protons distribution affects pH-dependent processes. Therefore, high local pH value, on the one hand, suppresses HER evolution in time and, on the other hand, inhibits pH-dependent *CO protonation (C₁ product formation mechanism) [112,113]. Since CO dimerization pathway is not pH-dependent, C₂ product formation is not disturbed by the high local pH and consequently ethylene selectivity is enhanced over OD-Cu. This effect can be empowered by limited ion diffusion in highly roughened surfaces, such as densely packed nanowires. Ma et al. [114] reported that length and density of Cu NW formed in Cu redox modification altered ion diffusion along with CO₂RR selectivity to C₂ products. Additionally, selectivity to ethylene was rising when the reaction was catalyzed by material with longer and denser NWs, hence, while ion mobility was hindered to a higher extent.

In the subject of OD-Cu electrocatalysts used in CO₂RR, one characteristic of this material remains a debatable matter, namely the role of subsurface oxygen. Scientific literature provides proposed mechanisms for the influence of residual/subsurface oxygen on CO₂RR intermediates adsorption, however, its stability in reductive conditions is frequently undermined [115]. Due to experiments and calculations conducted by Favaro et al. [116] presence of oxygen incorporated to Cu structure during oxidative pre-treatment impacts CO₂ adsorption on Cu (111) surface. As reported, CO₂ molecule can be adsorbed in two configurations: physisorbed linear CO₂ and chemisorbed bent CO₂, whereas, the molecule transfers from physisorbed to chemisorbed state in order to undergo further reduction. According to the theoretical simulations, both CO₂ linear physisorption and its subsequent conversion into chemisorbed bent form was thermodynamically facilitated when system contained 1:4 O to Cu ratio. This result implies the significance of subsurface oxygen in initial CO₂ activation. Eilert et al. [117] stated that the presence of subsurface oxygen alters CO₂ adsorption due to its electronegative nature. By combining findings of theoretical simulation and experimental techniques it was proposed that oxygen incorporated into Cu subsurface lowers charge density at the catalyst surface by attracting electrons towards bulk of the material. As a result, δ-repulsion between approaching CO₂ molecule and Cu surface are weakened. This consequently leads to stronger CO₂ adsorption and increases population of *CO species. Copper catalyst surface densely covered by adsorbed CO was proven to favor CO dimerization mechanism that shifts CO₂RR selectivity to C₂ products.

Great catalytic performance of oxide-derived copper electrodes in transforming CO₂ to C₂₊ products inspires researchers to constantly explore and develop new methods for OD-Cu synthesis. The plethora of protocols for redox copper modification can be categorized in accordance to oxidation process that Cu foil was subjected to. The most commonly used methods for forming oxide layer on copper surface are thermal oxidation [118,119], chemical oxidation [120], and electrodeposition [121,122]. In order to retrieve Cu metallic active sites oxidated nanostructures undergo subsequent partial or complete reduction. Kanan et al. [123] achieved thick Cu₂O film by annealing copper foil at different temperature and tested the materials in CO₂RR. It was found that thermal treatment at 130 °C did not cause significant changes in catalytic performance when compared to polycrystalline Cu. When annealing temperature was risen to 500 °C, 3 μm thick oxide film was formed on copper surface. This modification improved catalyst performance in CO₂RR by achieving higher activity at lower overpotential. Generally, copper electrodes that underwent high-temperature treatment indicate significant enlargement of ECSA that is abundant with surface defects. Frequently, those features are highlighted as morphological changes behind high efficiency of CO₂RR catalyzed by thermally

oxidized copper. On the other hand, electrodeposition method leads to formation of OD-Cu catalyst with ECSA that is typically smaller than in thermally oxidized materials. It is due to formation of less roughened morphologies, such as nanoparticles and nanoprisms [124]. Nevertheless, despite relatively small ECSA, materials obtained in electrodeposition method were found to impactfully enhance C_2 selectivity during CO_2RR [125]. Another technique worth noting for OD-Cu preparation is O_2 -plasma oxidation of the metal substrate [126,127]. Plasma treatment appears to be a versatile method that enables controllable modification of copper surface in order to tune its reactivity and C_{2+} selectivity in the process. Mistry et al. [126] applied H_2 -plasma and O_2 -plasma approach to activate surface of polycrystalline Cu catalyst for CO_2RR . It was reported that morphology of OD-Cu can be tuned by altering plasma power and exposure time. Furthermore, O_2 -plasma treatment resulted in incorporation of O atoms into subsurface Cu layers. Morphological changes and presence of subsurface oxygen led to significant C_{2+} selectivity enhancement for plasma-treated OD-Cu when compared to bare Cu foil. The ethylene faradaic efficiency obtained for CO_2RR catalyzed by this material reached 60% at -0.9 V vs. RHE ($\sim 20\%$ for Cu).

Oxide derived copper surface with highly developed surface area attained in controllable manner can be also achieved by anodic electrooxidation process. Growth of oxide/hydroxide layers on copper surface can be steered by tuning process variables, such as: electrolyte concentration and pH, temperature or applied potential. Xie et al. [58] reported CO_2 reduction over electrooxidized copper catalyst. In their work, authors generated 3D-structured CuO nanoflowers (Figure 4a) via pulsed electrochemical oxidation in alkaline environment. Electropolished copper foil was subjected to chronoamperometric treatment in 3.5 M NaCl and 0.1 M NaOH containing solution with three electrode configurations (Ag|AgCl reference electrode and Pt counter electrode). In oxidation cycles anodic (0.2 mA cm^{-2}) and cathodic (0.0 mA cm^{-2}) currents were applied consecutively (10 s and 2 s respectively) for 36 min. The procedure led to formation of cupric oxide chrysanthemum-like structures on copper surface. Electrocatalytic tests were performed in 0.1 M $KHCO_3$ electrolyte within potential range of -1.6 V to -0.6 V (vs. RHE). As reported, copper material with electrochemically developed superficial nanostructure indicated improved performance in catalyzing CO_2RR when compared to pristine Cu foil. Total current density for pre-prepared copper was higher within the whole range of applied potentials. It was due to significantly larger specific surface area of nanostructured copper. Besides well-developed surface area, growth of passive oxide layer on copper and subsequent reduction in reaction medium allowed creating numerous low-coordination defects that lower free adsorption energy of adsorbates in C_2 products formation. As confirmed by selectivity study, nanostructured Cu favored production of ethylene over methane, whereas polycrystalline Cu indicated opposite trend. Stability tests conducted at -1.3 V (vs. RHE) showed that C_2H_4 was a dominant product over CH_4 for 9 h with maximum Faradaic efficiency for C_2H_4 of ca. 20% (Figure 4b).

More currently, Dai et al. [128] reported protocol for pulse copper anodization using square-wave electrochemical redox treatment. In their approach, oxidation and reduction potentials (-0.45 V and -0.75 V vs. SCE) were applied consecutively to ultrapure copper foil in concentrated KOH. Catalyst preparation was conducted at 40°C , $\text{pH} = 13.7$ with addition of lactate ions in frequency of 5 redox cycles in 1 s. During one redox cycle copper followed transformation sequence: $\text{Cu} \rightarrow \text{Cu}(\text{OH})_2 \rightarrow \text{Cu}_2\text{O}/\text{CuO}$ and eventually underwent reduction to its metallic form. After multiple rapid redox cycles carried out for 0.5 to 10 h copper was roughened with surface layer of Cu_2O (Figure 5).

Copper oxide grown during the synthesis was in a form of nanoparticles (Figure 4g) which size depended of anodization time. As prepared catalyst was used for formate production in CO_2RR in 0.5 M $KHCO_3$ at -0.64 V vs. RHE. Prior to electrocatalysis, bicarbonate electrolyte was saturated with various pressure of CO_2 in a range of 1–60 atm. Since cathode in such electrochemical systems governs at least two competitive reactions, CO_2RR and HER, high CO_2 saturation favors CO_2RR . High suppression of HER with simultaneous improvement of CO_2RR was observed when CO_2 pressure was equal or higher than 45 atm. Under those conditions, anodized copper electrode indicated exceptionally high selectivity in CO_2RR towards formate production reaching 97.7% faradaic efficiency of this product.

To confirm Cu_2O significance and contribution to this result, oxide phase was monitored during the reaction. It was found that Cu_2O was slowly undergoing reduction and in 20 h 80% of oxide phase was reduced. Decrease in Cu_2O content impacted formate production reaching 84% FE when catalyst contained 20% of initial Cu_2O (Figure 4h).

In another study [93], the role of copper oxide in CO_2RR was intensively investigated by comparing polycrystalline copper with three oxide-derived catalysts prepared via different synthesis procedures. Surface oxidized layer was achieved by anodization, thermal annealing, and electrodeposition yielding three various CuO_x nanostructures: nanoneedles (NN), nanoparticles (NP), and nanocrystals (NC), respectively. Anodizing process of Cu foil was carried out in 2 M KOH solution with 2 electrode configurations (graphite counter electrode) for 5 min at constant current density (7 mA cm^{-2}). The process led to formation of $\text{Cu}(\text{OH})_2$ which was subsequently thermally converted into Cu_2O NN (Figure 4c). Electrocatalytic tests were performed in 0.1 M KHCO_3 electrolyte at constant current density and monitored using standard gas chromatography (GC) technique and operando selected-ion flow tube mass spectrometry (SIFT-MS). Results indicated that reduction of Cu^{2+} to Cu^0 is kinetically preferred reaction. Therefore, CO_2RR (and hydrogen evolution reaction, HER) is not occurring until Cu_2O is completely reduced. Nevertheless, authors stated that residual oxygen can be present in the system but not in a form of copper oxide. Electrocatalytic tests showed similar performance of OD-Cu materials in CO_2RR at constant current density (adjusted to ensure approximate potential of -0.8 V vs. RHE). Application of all the OD-Cu catalysts shifted selectivity of the process towards C_{2+} products formation. Catalyst prepared by electrochemical oxidation exhibited slightly higher affinity to C_{2+} products than other OD materials (Figure 4d). A study showed that OD-Cu catalysts led to a high C_2/C_3 ratio which was assigned to three features of OD-Cu catalysts: well developed geometric surface area, numerous surface defects that support CO adsorption, and increase of local pH value. High local pH originated from increased concentration of OH^- ions generated when protons from water underwent CO_2RR and HER. As aforementioned, high local pH enhances CO dimerization on copper at low overpotentials [129,130].

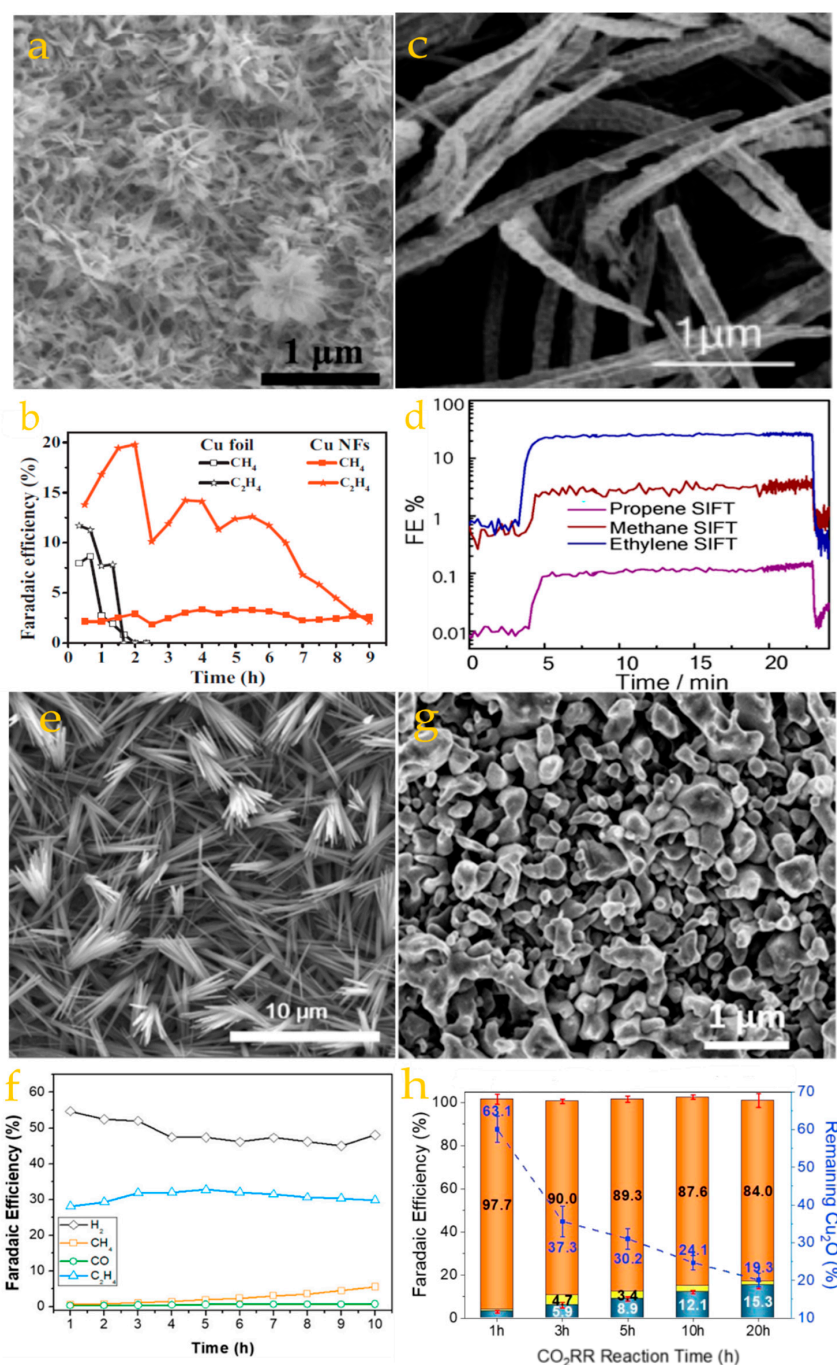


Figure 4. Collective results of morphology analysis (SEM images: (a,c,e,g)) and CO₂RR product distribution in time (b,d,f,h) for anodically oxidized copper based catalysts: (a) SEM image of nanoflower (NF) OD-Cu structure and (b) CO₂RR results for OD-Cu NF and Cu at -1.3 V vs. RHE in 0.1 M KHCO₃ reproduced from [58] © 2014 Elsevier Ltd.; (c) SEM image of nanoneedle (NN) OD-Cu structure and (d) constant current CO₂RR selectivity results of OD-Cu NN in time at -10 mA cm⁻² in 0.1 M KHCO₃ reproduced from [93] © 2018 American Chemical Society; (e) SEM image of nanowire (NW) structure OD-Cu and (f) CO₂RR results for OD-Cu NW at -1.05 V vs. RHE in 0.1 M KHCO₃ reproduced from [106] © 2018 American Chemical Society; (g) SEM image of OD-Cu nanoparticles (NP) morphology and (h) CO₂RR results for OD-Cu NP at -0.64 V vs RHE, under 45 atm. CO₂ in 0.1 M KHCO₃. Reproduced from [128] © 2020 American Chemical Society.

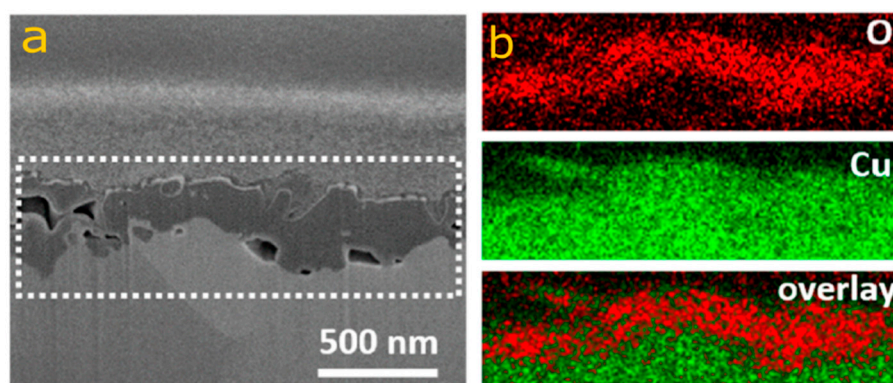


Figure 5. SEM cross-section image of OD-Cu catalyst prepared via square-wave electrochemical redox treatment (a) and its EDX mapping (b) showing oxide layer on copper surface. Reproduced from [128] © 2020 American Chemical Society.

The significance of oxygen in OD-Cu catalysts was highlighted by Lee et al. [106] in their study on anodized copper electrode for CO₂RR. Copper oxidation was conducted in 3 M KOH aqueous solution for 1 min at constant current density (10 mA cm⁻²). Applied conditions led to formation of Cu(OH)₂ nanowires morphology on the copper foil surface (Figure 4e). Subsequently, anodized material was subjected to electroreduction in CO₂RR medium: CO₂ saturated 0.1 M KHCO₃. To study the influence of pre-reduction step in CO₂RR over OD-Cu the catalyst was exposed to quick and slow reduction process. Samples of anodized copper were exposed to high and low potential (−4.0 V and −1.15 V vs. Ag|AgCl) for 10 and 100 min, respectively. It was found that pre-treatment conditions impacted catalyst specification and consequently its yield in CO₂RR. The overall charge that was delivered to the sample during quick electroreduction was an order of magnitude higher than that in the slower process. Rapid and intense reduction introduced more drastic changes in macroscopic appearance of the sample causing nanowires collapse. However, after CO₂RR microscopic morphology of both samples did not differ in a significant manner which implied that nanowires orientation was not a contributing factor in CO₂RR performance. Further investigation of slowly and rapidly reduced samples provided more detailed insight into samples diversity. Surprisingly, due to X-ray diffraction results, slow reduction at lower applied potential showed better effectiveness in reducing Cu(OH)₂. Therefore, rapidly reduced catalyst was more abundant in mixed copper valences (Cu⁰, Cu⁺ and Cu²⁺). The result was confirmed by X-ray photoelectron spectroscopy investigation. As it was found, oxygen to copper ratio (O/Cu) in rapidly reduced sample was 1.15, whereas O/Cu value reached only 0.10 in slowly pre-treated material. Those dissimilarities of materials pre-treated in contrasting conditions altered their ability to catalyze CO₂RR. Anodized copper indicated high selectivity towards ethylene in comparison to bare copper foil which led to methane formation. Additionally, it was found that shorter pre-treatment at higher applied potential enhanced catalyst selectivity and stability to a higher extend than longer and less intense process. Ethylene faradaic efficiency rose to almost 40% with rapidly pre-treated anodized copper (FE methane < 1%) and 30% with slowly reduced sample (FE methane~7%). Catalytic performance of reduced OD-Cu electrodes is also shown in Table 2. Besides selectivity improvement towards C₂ product, rapid pre-reduction at harsh conditions remarkably extended material durability in CO₂RR. Catalyst remained stable for 10 h on stream at −1.05 V vs. RHE (Figure 4f). As concluded, enhanced catalytic ability of rapidly reduced sample to reduce CO₂ into ethylene resulted from more diverse morphology that contained various copper valences, higher oxygen content, and surface defects generated during harsh condition pre-treatment.

Table 2. Collective results of CO₂RR catalyzed by electrochemically oxidized copper-based catalysts referenced in this section.

Morphology	Synthesis Method	Electrolyte	Potential [vs. RHE]	Faradaic Efficiency			Ref.
				C ₂₊	C ₁	Formate	
CuO nanoflowers	electrochemical pulsed oxidation	0.1 M KHCO ₃	−1.3 V	9%	4%	30%	[58]
Cu ₂ O nanoparticles	square-wave electrochemical redox treatment	0.1 M KHCO ₃ 45 atm. CO ₂ saturated	−0.64 V	-	-	98%	[128]
CuO _x nanoneedles	anodization	0.1 M KHCO ₃	−0.8 V	43%	<1%	2.4%	[93]
CuO _x nanocrystals	electrodeposition	0.1 M KHCO ₃	−0.8 V	38%	<1%	12%	[93]
CuO _x nanoparticles	thermal annealing	0.1 M KHCO ₃	−0.8 V	21%	-	-	[93]
Cu foil	-	0.1 M KHCO ₃	−0.8 V	4%	47%	-	[93]
CuO _x nanowires (collapsed after reduction)	anodization followed by rapid reduction (10 min at −4.0 V vs. Ag/AgCl)	0.1 M KHCO ₃	−1.05 V	38%	<1%	-	[106]
CuO _x nanowires (collapsed after reduction)	anodization followed by slow reduction (100 min at −1.15 V vs. Ag/AgCl)	0.1 M KHCO ₃	1.05 V	29%	7%	-	[106]
CuO _x nanowires	anodization	0.1 M KHCO ₃	−1.08 V	38%	1.3%	-	[106]
Cu foil	-	0.1 M KHCO ₃	−1.08 V	15%	24%	-	[106]

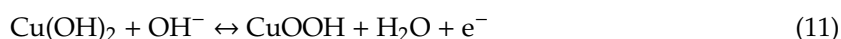
4. Direct Methanol Fuel Cell

Over past few decades direct methanol fuel cells (DMFCs) have been extensively studied as promising energy conversion devices with a simple set-up [131]. Direct methanol fuel cells have numerous desired advantages, including: high energy conversion efficiency, low operating temperature, and low pollutant emission. Storage and transportation of liquid methanol, used as fuel in such cells, is much safer than hydrogen, used in hydrogen proton exchange membrane fuel cells. Moreover, methanol oxidation does not include cleavage of C-C bond, leading to faster anodic reaction rates. Although the first small scale cells were commercially available, the development of technology to produce large-scale and cost-effective DMFCs is still a huge scientific challenge. The main issues in DMFCs design development that have to be addressed are: sluggish kinetic rates of oxygen evolution reaction, stable electrocatalytic activity, long-term durability of the catalyst, and achieving a high current density. A great deal of research is aimed at development of the electrode materials at which the typically large overpotential of methanol oxidation is lowered [132].

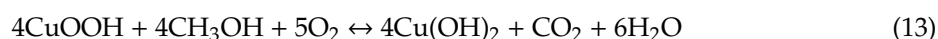
More recently copper and copper-derived materials attracted scientific interest as anodes for DMFCs, due to their high sensitivity and reactivity toward oxygen [133]. Copper is much less expensive and abundant in nature as compared with precious elements with superior electrochemical activity, such as Pt, Ru, and Pd [134]. Heli et al. [132] for the first time reported Cu as advantageous—in terms of cost-efficiency, ease of handling, and conductivity—material for methanol oxidation in alkaline solution. The methanol oxidation started at potential of 550 mV vs. Ag|AgCl through a mediated electron transfer mechanism catalyzed by Cu^{III} species formed at the same potential region. Panah et al. [133] showed, that the morphology of the Cu-derived anode is an important factor for the efficiency of the catalyst in the methanol fuel cell. They pointed out that the cyclic voltammetry polarization in 1 M NaOH led to increased surface roughness of Cu, due to formation of copper oxide layer, and subsequently increased

electrocatalytic performance for ethanol oxidation in alkaline medium. Therefore, it is not surprising that the copper-derived anodes have been already reported in literature for oxidation of methanol.

Methanol oxidation plays an important role of masking for highly-efficient hydrogen production from water electrolysis [135]. The oxidation of the methanol requires formation of CuOOH at the surface of Cu-derived electrode according to (11) and (12):



In the presence of methanol, the subsequent reaction occurs (13):



It is quite reasonable to assume that only the C^{2+} sites that got oxidized before methanol oxidation or only the Cu^{3+} sites that got reduced after methanol oxidation are the actual catalytically available Cu sites for methanol oxidation.

Similarly to those used for CO_2 reduction reaction, copper oxide electrodes for methanol oxidation were mainly obtained by hydrothermal method [136], however other methods have been also reported, such as reactive radio-frequency magnetron sputtering [137], electrodeposition and calcination [134] or anodization [135]. On the one hand, direct synthesis of the electrocatalytic material on the Cu substrate enhances mechanical adhesion, leading to fast charge-transfer between the oxide film and the current collector, without peeling off the active material [138,139]. On the other hand, such methods of synthesis do not require binding agent and support material.

El-Said et al. [140] reported hydrothermal method of synthesis of CuO nanoparticles (NPs) at indium tin oxide (ITO), however such electrode has been proven to be not suitable as anode for methanol oxidation in alkaline media. In acidic media CuO NPs@ITO exhibited long-time stability and retained 96.4% of its efficiency after 100 cycles. Xie et al. [141] prepared Cu(OH)_2 nanowire (with diameter in a range of 300–400 nm) array electrode at the surface of copper foam by wet chemical reaction. The Cu(OH)_2 nanowire array at Cu foam electrode was not efficient to catalyze the OER as it needed overpotential of 440 mV vs. SCE to obtain the current density of 50 mA cm^{-2} . Pawar et al. [136] reported Cu(OH)_2 and CuO nanowires array electrodes, prepared by chemical oxidation and annealing, for methanol electrooxidation. The Cu(OH)_2 nanowires were prepared at the surface of Cu by chemical oxidation in an alkaline medium (2.5 M NaOH and 1.25 M $(\text{NH}_4)_2\text{S}_2\text{O}_8$) at room temperature. The Cu(OH)_2 nanowires were transformed to CuO nanowires by annealing in air at 300 °C. The Cu(OH)_2 nanowires were 200–250 nm in diameter and 2 μm in length, however the CuO nanowires' dimensions were reduced in the process of annealing. As it was mentioned above, nanowires prepared by in-situ growth at the Cu substrate facilitate fast electron transfer between the current collector and the electro-catalyst with enhanced mechanical adhesion. The oxidation of methanol was performed in 1 M KOH and 0.5 M methanol solution. Both electrodes showed maximum current density above 100 mA cm^{-2} at 0.6 V vs. SCE and good long-term (up to 1800 s) electrochemical stability during methanol oxidation. The onset potential values were around 0.4 V vs. SCE. Pawar et al. [137] reported the use of singular phase materials of Cu_2O or CuO prepared by controlling the oxygen flow rate during reactive radio-frequency magnetron sputtering of copper, for electrooxidation of methanol. The measured onset potential in 1 M KOH and 0.5 M methanol solution, for both electrodes was ca. 0.42 V vs. SCE. However, the anodic current density of the CuO electrode was much higher than that of the Cu_2O electrode. This indicated that the CuO electrode is more electro-catalytically active as compared to the Cu_2O electrode. After the addition of 0.5 M methanol, the current densities for the Cu_2O and CuO electrodes were about 10 and 16 mA cm^{-2} respectively, in the steady-state region and did not show any decay up to 3000 s.

Up to date lowest onset potential of methanol oxidation of around 0.38 V Ag|AgCl in 1 M KOH + 0.5 M methanol (scan rate 10 mV s^{-1}) was reported at CuO@Ni foam catalyst prepared by copper electrodeposition at Ni substrate and calcination at $400 \text{ }^\circ\text{C}$ [134]. Current density recorded in the presence of methanol was 130 mA cm^{-2} , which constituted 10 fold increase as compared with solution without methanol addition. Current density reported by Roy et al. [134] is higher than the ones reported earlier by other authors [133,135,140], which can be attributed to relatively higher electrochemically active surface area due to the use of Ni foam. Such electrode showed 95% retention of the current density after 2000 s.

Interestingly, the use of Cu-derived electrode obtained by electrochemical copper oxidation as an electrode for methanol oxidation has been reported to date only once (Figure 6a) [135]. Anantharaj et al. [135] showed a swift potentiostatic method of copper electrooxidation in 1 M KOH for fast fabrication of 5–7 μm long nanoneedle array of $\text{Cu}(\text{OH})_2\text{-CuO}$ on Cu foil within 100 s at $-60 \text{ mV vs. Hg|HgO}$ (Figure 6b). Such electrode was screened toward electrochemical oxidation of 0.5 M methanol in 1 M KOH, and at current density of $70 \pm 10 \text{ mA cm}^{-2}$ at 0.65 V vs. Hg|HgO was recorded. The measured current density increased with duration of anodization and stabilized after 50 s (Figure 6). The addition of 0.5 M methanol lowered the overpotential at 10 mA cm^{-2} by 334 mV, when compared to the reference test without methanol. The enhanced activity was attributed to formation of the high active surface area. Moreover, such electrode exhibited excellent stability for over 6 h of potentiostatic electrocatalytic methanol oxidation while retaining the charge-transfer resistance, nonetheless some changes in the morphology of the material was evident. Anantharaj et al. [135] found that $\text{Cu}(\text{OH})_2\text{-CuO/Cu}$ electrode had 2.64×10^{16} electrochemically accessible Cu sites for methanol electrooxidation. This value was used to calculate turnover frequency (TOF). The TOF for methanol oxidation increased with the increasing potential and the highest value (3.5 k s^{-1}) was observed at the vortex potential of 0.65 V vs. Hg|HgO, OH^- . This is the highest TOF value ever reported for a nonprecious methanol oxidizing electrocatalyst. Authors also pointed out, that the methanol oxidation at the electrode material exhibited Nyquist plot characteristic for a totally charge-controlled reaction, indicating, that the methanol oxidation is controlled by reaction kinetics rather than the diffusion of methanol. However, the oxidation of Cu^{2+} to Cu^{3+} is a diffusion-controlled reaction. One can suspect that further increase of the electrode surface, e.g., by anodizing the foam-like Cu substrate could lead to even more impressive results.

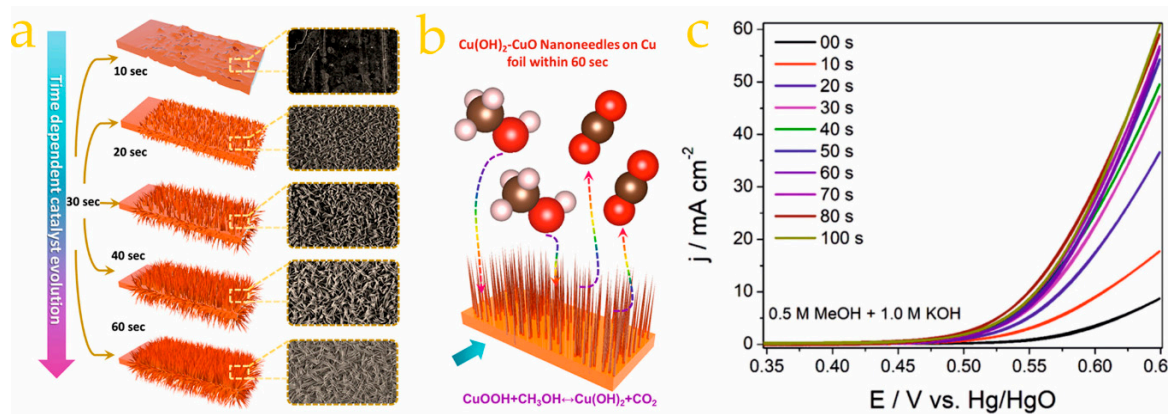


Figure 6. (a) Scheme of $\text{Cu}(\text{OH})_2\text{-CuO}$ formation during potentiostatic electrooxidation of copper in 1 M KOH. (b) Scheme of methanol oxidation at the surface of as prepared electrocatalyst. (c) Voltammograms of methanol electrooxidation at the surface of the pristine Cu foil in comparison with the Cu foils anodized for different time periods. Reproduced from [135] © 2020 American Chemical Society.

It is important to point out, that although the Cu-derived electrodes exhibit multiple advantageous features for DMFCs (discussed earlier), the onset potential values of methanol oxidation reported to date are too high to directly exploit these electro-catalysts in practical application.

5. Glucose Sensing

Anodic copper oxides are considered as outstanding electrodes in numerous reactions. Oxidation of organic compounds, at specific potential, on anodically grown CuO_x is also a foundation of non-enzymatic sensing. Literature study reveals that anodic copper oxides have been also proven to be reliable glucose sensors.

The electrodes for glucose sensing can be divided into two groups: enzymatic and non-enzymatic. Although the commercially available enzymatic biosensors are commonly applied and superior in terms of sensitivity and selectivity to non-enzymatic biosensors, their use is limited by higher costs and poor stability over time. Due to low cost and good chemical activity, Cu-derived nanostructured electrodes have been explored as promising non-enzymatic electrodes for sugars oxidation [142]. Such nonnoble electrodes exhibit lower overpotential for the redox reaction, however accomplishing their high selectivity, sensitivity and refractoriness to surface poisoning is still a challenge [143]. Up to this point, reports considering Cu-derived glucose sensors point out that their performance, detection range and detection limit are influenced by the particle shape and morphology, and therefore indirectly by the synthesis method (See Table 3). One general approach of CuO glucose sensors preparation is direct immobilization of copper oxide nanoparticles at the surface of supporting material (e.g., glassy carbon). Due to weak adhesion, the CuO nanostructures can be easily detached from the surface, leading to unreliable results. To resolve this issue, use of polymer binder, i.e., Nafion[®], was proposed [144,145]. Another method uses in-situ preparation of copper oxides at the surface of Cu substrate by wet-chemical method [146] or thermal oxidation [147]. Such samples provide better adhesion of the oxide to the substrate surface, however large-scale, reproducible synthesis of uniform material remained challenging. Finally, electrochemical oxidation (anodization, cyclic voltammetry polarization [148], etc.) was used as a method of direct fabrication of the copper oxide layer on the copper surface as a strategy for highly sensitive and stable glucose sensor development.

Ashok et al. [145], in their work, pointed out that not only the morphology of the particles, but also composition and crystallinity of the material, influence sensor performance. Previous reports [144,155] are in line with these findings. Lu et al. [153] showed that the electrooxidation conditions (current density and concentration of electrolyte) influenced morphology and composition of the obtained material, what was accompanied by changes in the electroactivity toward glucose oxidation. Additionally, Li et al. [143] pointed out that there is an optimal thickness of the Cu-derived layer that provides the best analytical response due to advantageous balance between: (i) diffusion of the glucose and products to and from the electrode surface, (ii) high number of active sites at highly developed surface, (iii) electron transport from oxide layer to conductive substrate.

Table 3. Overview of selected reports on non-enzymatic Cu-derived glucose sensors performance.

Material	Method of Synthesis	Morphology	Linear Response Range	Limit of Detection	Sensitivity	Ref.
CuO@GC	Wet-chemical method	Nanowires with nanoflower particles	1–850 μM	0.25 μM	2062 $\mu\text{A mM}^{-1} \text{cm}^{-2}$	[145]
CuO/CuO _x /Cu	Electrooxidation: potentiodynamic	Rough and porous	Up to 15 mM	0.05 μM	1890 $\mu\text{A mM}^{-1} \text{cm}^{-2}$	[149]
Cu ₂ O@Cu	Galvanostatic anodization and annealing under Ar flow	Flower-like nanowires with length > 5 μm	1 μM –2 mM	0.58 μM	4060 $\mu\text{A mM}^{-1} \text{cm}^{-2}$	[150]
Cu _x O@Cu	Electrooxidation: potentiodynamic	Spike covered nanowire array	10 μM –7 mM	10 μM	1210 $\mu\text{A mM}^{-1} \text{cm}^{-2}$	[148]
CuO @SPE	Electrooxidation: potentiodynamic	Flower-like nanoparticles	0.5 μM –15 mM	0.06 μM	3225 $\mu\text{A mM}^{-1} \text{cm}^{-2}$	[151]
Cu _x O@Cu nanoparticles@ Cu foil	Thermal oxidation	Nanowire array	Up to 4.0 mM	49 μM	1620 $\mu\text{A mM}^{-1} \text{cm}^{-2}$	[147]
Cu _x O@Cu	Potentiostatic anodization	Microparticles 100–800 nm	25 μM –9.05 mM	14.3 μM	452.4 $\mu\text{A mM}^{-1}$	[152]
CuO@ Cu foam	Hydrothermal and annealing in air	Nanowires and nanoflowers	0.10 μM –0.50 mM	0.02 μM	32330 $\mu\text{A mM}^{-1} \text{cm}^{-2}$	[146]
Cu ₂ O@ Cu foil	Galvanostatic polarization	Cubic nanoparticles 30–150 nm in diameter	0.1–1 mM	2.57 μM	2524.9 $\mu\text{A mM}^{-1} \text{cm}^{-2}$	[153]
CuO	Wet-chemical method/microwave assisted	Microparticles with sandwich-like structure	Up to 3.2 mM	~1 μM	5342.8 $\mu\text{A mM}^{-1} \text{cm}^{-2}$	[144]
Cu ₂ O@Cu foil	Potentiostatic polarization	Octahedron microcrystals	0.05–6.75 mM	37 μM	62.29 $\mu\text{A mM}^{-1}$	[154]
CuO	Galvanostatic anodization	Nanotube array with 300 nm diameter and 15 μm length	5 μM –3.0 mM	0.1 μM	1890 $\mu\text{A mM}^{-1} \text{cm}^{-2}$	[155]
CuO UPN	Wet-chemical method and annealing in air	Carnation-like particles 2.5 μm in diameter composed of 15 nm thick nanosheets	3 μM –5.3 mM	0.098 μM	3150 $\mu\text{A mM}^{-1} \text{cm}^{-2}$	[156]
Cu/Cu ₂ O/CuO	Aerosol furnace reactor assisted synthesis	Hollow spheres with diameter of 0.05–3 μm	0.5 μM –30 mM	0.39 μM	8726 $\mu\text{A mM}^{-1} \text{cm}^{-2}$	[157]
Cu ₂ O	Galvanostatic anodization and annealing	Porous nanotube or nanorod array with diameter of 40–70 nm	Up to 0.1 mM	0.015	5792.7 $\mu\text{A mM}^{-1} \text{cm}^{-2}$	[158]

GC—glassy carbon; CV—cyclic voltammetry; CuO_x—copper oxalate; SPE—screen printed electrode UPN—ultrathin porous nanosheets.

Babu et al. [149] reported formation of CuO/CuO_x (copper oxalate) modified Cu electrode by potentiodynamic anodization by cyclic voltammetry (CV) in potassium oxalate solution and its successful application as a glucose sensor. Its performance was examined in both in water solution and blood serum with good linearity in a range of 0–15 mM as well as satisfactory selectivity (compared with ascorbic and uric acid) and reproducibility (variation less than 1%), over one month of storage (sensitivity lost 2.5% of its original current density response value). The limit of detection (LOD) of this nonenzymatic sensor was reported to be 0.05 μM, while the sensitivity was found to be 1890 μA mM cm⁻². CuO nanotube arrays, obtained by anodization in 3.0 M KOH solution at constant current density of 3 mA cm⁻² for 25 min in three-electrode system followed by heating at 200 °C for 3 h under nitrogen atmosphere, showed similar sensitivity and negligible loss of electroactivity (95% retention after 32 days) [155]. The improvement of the current density as compared with CuO powder, indicated that glucose oxidation strongly depends on the surface morphology of the electrodes. The superior sensitivity of the CuO nanotube arrays sensor is acknowledged to the ideal electrode architecture, which increase the electroactive surface area and accelerate the mass diffusion to the active sites. Additionally, in-situ fabrication of such CuO array sensor avoids the use of polymer binders. Dhara et al. [151] showed that CuO nanoflower glucose sensor prepared by potentiodynamic electrooxidation in 0.5 M NaOH exhibited even higher sensitivity of 3225 μA mM cm⁻² and LOD of 0.06 μM. It showed good selectivity towards glucose in presence of other commonly interfering analytes, such as ascorbic acid, acetaminophen, dopamine, uric acid, urea, creatinine, sodium chloride, and carbohydrates (fructose, maltose, galactose, and lactose) at their physiological concentrations. Interesting approach was reported by Fan et al. [148] as they used cyclic voltammetry to oxidized Cu nanowire array, prepared by electrodeposition of copper in the pores of anodic aluminum oxide membrane. As a result, Cu nanowires were covered with Cu_xO spikes, which significantly increased the active surface area of the electrode. The sensitivity was only 1210 μA mM⁻¹ cm⁻² in a range of 0.01–7 mM, and the response time was under 1 s. Such low sensitivity could be associated with the fact that the nanowires are densely packed, impeding diffusion of glucose and products of its oxidation.

Interestingly, a sample made of Cu₂O octahedron nanocrystals at Cu, prepared by anodization at 5 V applied potential for 5 min in mixed alcohol–water (1:1) solution containing 0.01 M benzoentricarboxylic acid and 0.1 M NaClO₄, showed higher LOD (37 μM) and lower sensitivity [154]. Conversely, Cu₂O micro- and nanocrystals decorated Cu electrode prepared by electrooxidation of copper in 3 M NaOH solution at constant current density of 1.415 mA cm⁻² for 300 s exhibited much better performance as a glucose sensor with LOD of 2.57 μM and sensitivity of 2524.9 μA mM⁻¹ cm⁻² [153]. Authors also pointed out that Cu₂O covered electrodes showed higher catalytic activity in oxidation of glucose than orthorhombic Cu(OH)₂ (in a form of nanotubes) obtained by anodizing at higher current density and lower NaOH concentration. More recently, Dat and Viet [150] reported preparation of Cu₂O nanowires at copper foil by galvanostatic anodization (3 M KOH, 6 mA cm⁻², 10 min) with subsequent calcination at 600 °C in Ar flow, which exhibited impressive sensitivity of 4060 μA mM⁻¹ cm⁻² with low LOD (0.58 μM) and good selectivity toward glucose in the presence of dopamine, uric acid, ascorbic acid, NaCl, and sucrose.

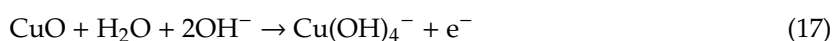
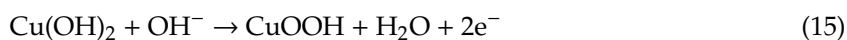
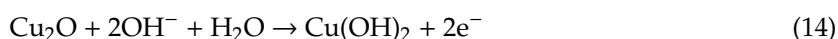
Zhang et al. [159,160] recently proposed use of Cu_xO/Ag₂O on Cu foam, prepared by galvanostatic anodization (15 mA cm⁻²) in 0.5 M KOH and subsequent annealing at 200 °C in air, however as prepared composites did not exhibit improved sensitivity, LOD, or linear range as above mentioned materials. However, it showed superior stability of 96.94% current density response after 30 days, as compared to original value. Interestingly, Cu₂O/CuO nanowires prepared by anodization (3 M NaOH, 6 mA cm⁻², 10 min) and annealing (600 °C in air), subsequently modified by CuS, exhibited sensitivity of 4262 μA mM⁻¹ cm⁻² in linear range 2 μM–4.1 mM of glucose and LOD of 0.89 μM, what was attributed to the increased surface area [161]. Up to date, the best results for electrooxidized Cu glucose sensors were reported by Jayasingha et al. [158]. Cu₂O nanotubes were prepared by anodization of copper foam in 3 M NaOH at 25 °C at constant current density 10 mA cm⁻², and subsequent annealing at 180 °C for 1 h in N₂ and 500 °C for 3 h in a tube furnace. As-prepared material exhibited sensitivity of

5792.7 $\mu\text{A mM}^{-1} \text{cm}^{-2}$ up to 0.1 M with extremely low LOD of 15 nM, and the response time under 1 s. The superior performance was attributed to distribution of the Cu_2O nanotubes grown on the entire surface of the copper foam, leading to high accessibility to glucose molecules. The electrochemical detection of glucose was however disturbed in the presence of fructose, sucrose and ascorbic acid. The stability of the material was moderately good, and the amperometric response was ca. 95% of its original value after 10 days.

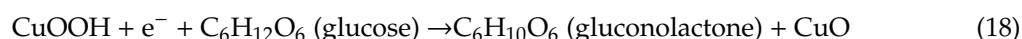
$\text{Cu/Cu}_2\text{O/CuO}$ hollow spheres, synthesized using aerosol furnace reactor, bounded to the GC surface using Nafion[®], exhibited uncanny sensitivity of 8726 $\mu\text{A mM}^{-1} \text{cm}^{-2}$ in a range of and LOD of 0.39 μM [157]. The main issue observed for this material was its stability, as the efficiency dropped by ca. 24% after 14 days (sensitivity of 6545 $\mu\text{A mM}^{-1} \text{cm}^{-2}$), therefore its commercial use is not practical.

To date, highest sensitivity toward glucose exhibited CuO nanowire array at Cu foam prepared by hydrothermal method and subsequently annealed at 180 °C in air for 2 h, i.e., 32,330 $\mu\text{A mM}^{-1} \text{cm}^{-2}$, with quite good reproducibility [146]. This material had also good stability, as the amperometric response was ca. 94.1% of the original current density value after 12 days.

Although the exact mechanism of electrooxidation of glucose at the surface of CuO , Cu_2O or Cu derived electrodes in alkaline medium is still under debate, the works of Marioli and Kuwana [162], and Wei et al. [163] put forward multistep process as follows. The initial oxidation of CuO , Cu_2O , and Cu(OH)_2 to CuOOH or Cu(OH)_4^- occurs, leading to formation of centers at Cu(III) state (14)–(17).



Subsequently, the deprotonation of glucose in an alkaline medium triggers isomerization to an enediol form which reacts with Cu(III) , and is oxidized to gluconolactone (18), and further hydrolyzes to more stable gluconic acid (19).



Alternatively, in alkaline medium, a 12-electron process can lead to cleavage of the C–C bond in glucose, resulting in formation of products with lower molecular weight, i.e., formate or carbonate [164].

Since the oxidation of the glucose occurs at the surface of copper oxide, very high sensitivity of sensors discussed in this undersection may be attributed to the synergistic effect of two significant factors, i.e., (i) the supreme electrocatalytic activity of the $\text{Cu(II)}/\text{Cu(III)}$ redox couple, and (ii) the highly developed surface of microporous structure [149]. It is well known that the electro-oxidation of glucose is a kinetically controlled sluggish reaction. The Faradaic currents associated with a kinetically-controlled electrochemical reaction are sensitive to the nanostructure of electrodes with large surface area. Obviously, the enhanced electroactivity for glucose oxidation on the highly porous electrode prepared by in-situ copper anodizing may be attributed to its high porosity, highly conductive matrix and large surface area which provides more active sites for the reaction and significantly enhances electron transfer and mass transport rate. It should be noted that the precise values of sensitivity should be considered carefully, as the real surface area of the electrodes is rarely determined, and their performance as glucose sensors is difficult to compare solely on the bases of the literature reports. Nonetheless, the systematic study on direct influence of the morphology, composition and structure on performance of Cu -derived glucose sensor has not been reported yet.

6. Organic Pollutant Photodegradation

Another emerging application of Cu-derived materials, formed by anodization, is photocatalytic degradation of water pollutants [165]. Photocatalytic degradation process of various environmental pollutants (i.e., organic dyes) using semiconductors has received considerable attention because of its low cost and high efficiency. Along with the widely used TiO_2 , ZnO , and V_2O_5 photocatalysts [166–168], the *p*-type Cu_2O semiconductor has also been employed due to its narrow band gap (2.17 eV) [169]. The Cu substrate provides a conductive path for the photo-generated electrons, preventing their recombination with photo-holes, therefore maintaining photocatalytic activity and stability. Although some novel $\text{Cu}_2\text{O}@Cu$ heterostructures prepared by electrodeposition and annealing have been reported for photodegradation of organic dyes [170], the copper oxide obtained by Cu mesh anodization proved superior activity in degradation of rhodamine B [165,171].

Yang et al. [170] reported enhanced photocatalytic degradation of rhodamine B by Cu_2O coated silicon nanowire arrays in presence of H_2O_2 . Cu_2O was formed by electrodeposition of copper and subsequent annealing. The photocatalytic activity of material was attributed to formation of *p-n* junction between *p*-type Cu_2O nanoparticles and *n*-type silicon nanowire array, which could effectively accelerate separation of photo-generated electron-hole pairs. The degradation rate of rhodamine B in the presence of H_2O_2 was 97.5% within 60 min, and apparent rate constant of degradation was 0.0611 min^{-1} .

Porous Cu_2O film, prepared by anodization (0.2 M ammonium chloride, 5 mA cm^{-2} , 600 s, room temperature) combined with foaming (immersion in H_2O_2 solution for 30 min) was used for photodegradation of negatively charged methyl orange, and showed superior activity when compared with microcrystalline Cu_2O due to its higher active surface area [172]. Cu_2O porous nanosheet arrays, prepared directly at the surface of Cu by chemical oxidation and subsequent calcination also showed improved photodegradation of methyl orange.

Li et al. [171] used 10 min anodizing in 0.5 M KOH at the constant current density of 5 mA cm^{-2} and subsequent calcination to fabricate $\text{Cu}_2\text{O}/\text{CuO}$ nanosheets at the surface of the nanoporous copper/bulk metallic glass (NPC/BMG), obtained in turn by dealloying of $\text{Cu}_{50}\text{Zr}_{45}\text{Al}_5$. Such material exhibited higher activity toward photodegradation of rhodamine B in the presence of H_2O_2 (99% degradation after 9 min), as compared with anodized in identical conditions: Cu plate (unwanted corrosion pits) and commercial Cu foam, where $\text{Cu}_2\text{O}/\text{CuO}$ nanosheets were much larger. This was attributed to the differences in the size of the Cu substrate skeleton, as the best results were obtained for the composites with ultra-fine nanosheet arrays. Moreover, prepared material retained 95.2% of photoactivity over 7 cycles. In further work, Li et al. [165] studied how the morphology of nanoporous copper and the conditions of galvanostatic anodization affected the morphology of Cu_2O . The anodization was performed in 0.5 M KOH solution at constant current density of 20 mA cm^{-2} for 1–20 min at 25°C at the same dealloyed material. Subsequently, as-prepared samples were annealed at 200°C for 2 h in the air atmosphere. At higher current density they observed gradual formation of nanowires gathered in nano-flower-like bundles. Sample prepared by 15 min-long anodizing showed 100% degradation of RhB after 5 min, with 96% retention over 7 cycles, which is the best stability reported to date for Cu-derived materials.

On the one hand, micro- and macroporous morphology of this material provides more surface area to absorb light and therefore produces more photo-generated electrons and holes. On the other hand, heterojunction of copper oxides and copper is beneficial for fast transfer of electrons and avoiding the recombination of electron-hole pairs. Finally, the Cu_2O nanowires gathered in nanoflowers with fan-shaped structure can offer ideal channels to transfer RhB molecules in solution. The mechanism of the RhB degradation at $\text{Cu}_2\text{O}@NPC$ was proposed in the Figure 7. The hydroxyl radicals ($\bullet\text{OH}$), formed from H_2O_2 in the presence of Cu_2O and visible light, are essential for the degradation of RhB. The rhodamine B molecules react with the hydroxyl radicals ($\bullet\text{OH}$) and finally are degraded.

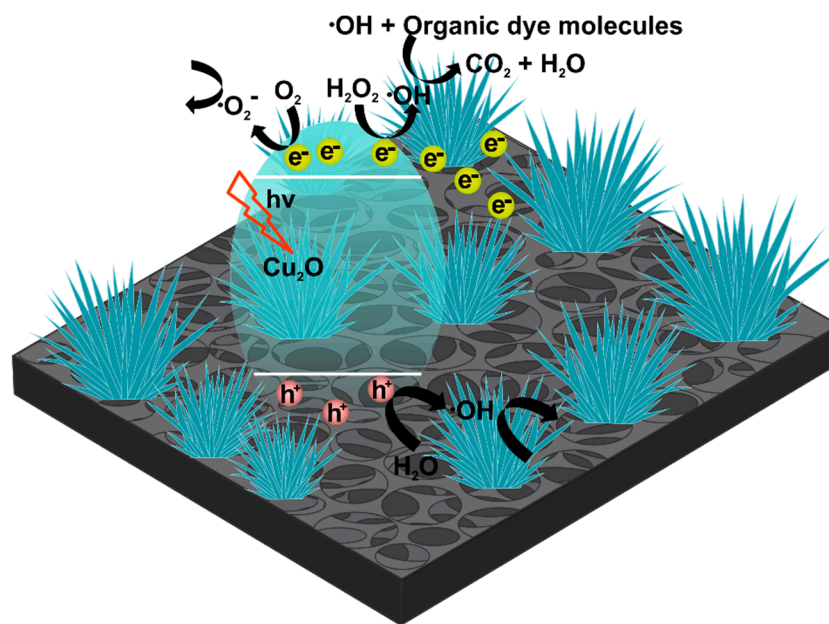


Figure 7. Schematic illustration of the possible mechanism for the RhB degradation by the Cu₂O@NPC composite. Figure adapted from [165].

7. Copper Oxides Photocathodes for Photo-Electrochemical (PEC) Water-Splitting Applications

Nowadays, one of the most promising alternatives to fossil fuels to attend the energetic demand is hydrogen fuel. The hydrogen can be produced via several processes like steam methane reforming, from biomass, biological processes, water electrolysis, photo-electrochemical (PEC) processes, among others [173]. PEC cells are sustainable devices that convert solar energy into hydrogen via the water-splitting reaction. Consisting basically of a photocathode, a photoanode, and an aqueous electrolyte, these devices are designed to absorb photons on the photoelectrode surfaces with sufficient energy to generate electron-hole pairs which separate and migrate to the electrodes/electrolyte interface where the hydrogen evolution reaction (HER) and oxygen evolution reaction (OER) take place. The electrochemical set up, where reactions are conducted is designed to carry out HER and OER separately in different cell compartments. Then the hydrogen gas can be collected for storage or used in a fuel cell to generate electric energy.

The overall water electrolysis reaction: $2 \text{H}_2\text{O} (\text{aq}) \rightarrow \text{O}_2 (\text{g}) + 2 \text{H}_2 (\text{g})$ requires 1.23 eV e^{-1} , however, potentials in 1.4–1.8 V range are used to obtain a significant amount of gas with conventional Pt electrodes [174]. Since semiconductors can intake part of this energy from the absorption of photons [174], these materials are considered as promising and sustainable alternative for Pt electrodes in hydrogen production by water splitting. In this sense, the hydrogen reduction from water discharge occurs at the photocathode surface, usually composed of a *p*-type semiconductor, whereas *n*-type semiconductors are used in the photoanodes, where oxygen from water is oxidized to O₂ [175,176].

The conduction band edge of *p*-type semiconductors is more negative than the potential required for HER. For this reason, these semiconductors are used as photocathode for PEC water-splitting. The *p*-type CuO and Cu₂O semiconductors with a 1.2–2.2 eV bandgap have been explored as photocathodes in PEC systems due to their attractive properties, like suitable conduction band position, strong redox capability, good conductivity, abundance, and non-toxicity [176–178]. The *p*-type characteristics of the copper oxides are usually ascribed to the copper vacancies and can be tuned by the synthesis method [179].

Bandgap values lower than 2.0 eV indicate that the semiconductor can absorb a larger part of visible light irradiation [175], which is an eligible criterion for economical photoelectrodes materials, in addition to the desired properties like high efficiency and long-term stability. The theoretical

solar-to-hydrogen (STH) efficiency for a Cu_2O photocathode with a bandgap of 2.0 eV is 18% [180,181] which is a promising result for a practical application of this material in PEC water-splitting systems. The higher stability and superior light absorption of CuO [73,181,182] turn the cupric oxide preferred for PEC applications than the Cu_2O . Stability of Cu_2O - CuO systems, in different architectures, was proven to be better than in the case of Cu_2O alone [67,175,181,183].

Despite these advantages, the copper oxides exhibit low resistance to photocorrosion in contact with the electrolyte and limited carrier diffusion length—factors that can reduce the overall performance of the PEC device and limit the practical use of this semiconductor as a photocathode in technological applications [181]. In this sense, different approaches are being used to overcome these limitations and improve PEC performance including: (i) the use of protective layers to enhance the oxide stability [182]; (ii) the fabrication of aligned nanostructures creating direct pathways for the photogenerated charges and increasing the surface area [178,181,183]; (iii) the manufacture of Cu_2O - CuO heterostructures for a rapid charge carrier separation, reducing the recombination of the photogenerated electrons and holes due to the energy level differences of the conduction and valence bands in the interface of the heterostructure layers [46,183].

Besides electrode architecture and morphology, structural parameters like the preferred crystallographic orientation and grain size can also influence the PEC efficiency [67,175]. Since these parameters depend on experimental conditions of the synthesis, a suitable choice of the synthetic route is pivotal to control composition, morphology, crystallography, and electronic structure of the copper oxides for PEC applications.

Currently, the development of copper oxides photocathodes for hydrogen production via PEC water-splitting is in its early-stages. Most of the studies are focused on the design of the synthetic routes in order to control the properties of the oxide and to improve its stability and photoconversion efficiency. Among these synthetic methods, the anodization of copper foils stands out for being a facile, scalable, time-efficient manufacturing process for the fabrication of 1D nanostructures such as nanowires, nanoneedles or nanoflakes [31,178,182]. In addition, it provides efficient metal back contact with the oxide, avoiding the use of binding agents [178].

Different strategies combining anodization and thermal treatments are being used to investigate the photoelectrochemical activity of the copper oxides by analysis of the electronic structure and photocurrent density measurements [67,175,178,181–183]. In general, these studies aimed to correlate composition, morphology, crystallographic orientation, and grain size with the electronic properties and, consequently, with the photocurrent response. To investigate the electronic structure of the semiconductor, Diffuse Reflectance Spectroscopy (DRS) and EIS coupled with Mott-Schottky analysis are used to extract the information about semiconductor bandgap, conduction band position, flat band potential, and charge carrier density.

It is important to emphasize it is difficult to perform a direct comparison between efficiency and photocurrent activities of the materials based on the actual literature devoted to PEC systems, since there is a lack of standardized procedure for PEC parameters evaluation. The photocurrent characterization is carried out under different conditions and the efficiency is usually determined using different models such as the applied bias photon-to-current efficiency (ABPE), incident photon-to-current efficiency (IPCE), absorbed photon-to-current efficiency (APCE), and solar-to-hydrogen conversion efficiency (STH) [180,184]. Hence, the overall efficiency is not standardized and can change depending on the experimental conditions.

Therefore, a general description of PEC systems involving copper oxides requires a more qualitative approach instead of a quantitative one. One exception to a comparative analysis is the study performed by Zimbovskii and Baranova [179] that performed a preliminary investigation of photocatalytic activity of Cu_2O layers on Cu deposited over Fluorine-doped Tin Oxide (FTO) substrates. In this case, since all electrodes were tested under the same experimental conditions, a direct comparison among different synthetic methods could be visualized. In this work [179], the authors compared three synthetic routes using copper substrates: (i) chemical oxidation of copper and thermal reduction; (ii) anodization

of copper and thermal oxidation; and (iii) hydrothermal synthesis. A fourth methodology using a different substrate, i.e., (iv) electrodeposition of copper over a FTO glass was also applied for comparison. They observed that the photoactivity of the synthesized electrodes increased in the following sequence: iv < iii < i < ii. The anodized oxide electrode exhibited a maximum photocurrent density of $-1.6 \text{ mA}\cdot\text{cm}^{-2}$ at $-0.6 \text{ V vs. Ag|AgCl}$ and quantum efficiency of 2.0% under irradiation of a 6300 K white light-emitting diode (100 mW cm^{-2}). The authors attributed this behavior of the anodized sample to the small diameter of Cu_2O microrods with a large surface area, which allowed an effective absorption of the incident light.

Regarding the studies focusing on anodized copper oxides in PEC applications, Table 4 depicts the photocathode architectures explored and the parameters extracted from photocurrent characterization, usually performed by LSV in a 3-electrode electrochemical cell under chopped light irradiation. In general, these copper oxides nanostructures are produced by anodization of Cu foil/films in alkaline media followed by heat treatment. John et al. [182] reported the growth of CuO nanoflakes by galvanostatic anodization of Cu foil in 3 M KOH solution followed by hydrothermal treatment at $100 \text{ }^\circ\text{C}$ (30 min, 1 h and 3 h, respectively) with a good PEC activity. However, to improve the photo-response without altering the phase and morphology of the CuO nanoflakes, the authors applied a rapid thermal treatment at $400 \text{ }^\circ\text{C}$ for 10 s. EIS and Mott-Schottky analysis revealed that this procedure increased the charge carrier density of the sample, resulting in a high photocurrent density (Table 4), with an efficiency of 2.35% (ABPE). The conduction band positions estimated from the bandgap were more negative than the water reduction potential, ideal for water splitting applications. The authors also compared the photocurrent results with other materials from the scientific literature to emphasize the superior photoactivity of the anodized material. Despite the remarkable results, the stability tests of the anodized photoelectrode showed decay in the photocurrent density over time which authors ascribed to the cathodic photocorrosion of CuO into Cu_2O .

In a subsequent report from the same research group [183], a core-shell heterostructure was synthesized in order to improve charge separation and reduce recombination. The Cu_2O nanostructures were produced by anodization of Cu foil in 3 M KOH solution at 10 mA cm^{-2} for 60 s and followed by annealing at $450 \text{ }^\circ\text{C}$ for 2 h. Then, the Cu_2O nanowires were thermally treated in diluted KOH solution for 10, 20, and 30 min to form CuO nanoflakes over Cu_2O nanowires. The authors observed that the $\text{Cu}_2\text{O}@Cu\text{O}$ nanowire/nanoflake heterostructure produced via controlled oxidation of the Cu_2O to CuO not only provided a fast charge separation but also offered a higher surface area for catalytic reactions, enhancing the performance of the photocathode.

By applying anodic oxidation, hydrothermal synthesis, and partial thermal oxidation, Mirzaei et al. [175] fabricated photoelectrodes over Cu substrate containing Cu_2O (majority) and CuO. Since (100) and (110) crystallographic planes of Cu_2O are more susceptible to photocorrosion [175], the synthesis was optimized to favor the preferred (111) orientation, which could be done by control of the hydroxyl and oxygen concentration on the surface as well the by control of the oxide growth rate. The resulting films possessed a nanosphere structure with significant photoactivity. Nevertheless, the sample with better photostability presented the lowest photocurrent density. The highest photocurrent response was obtained by the sample exhibiting the highest charge carrier density.

The influence of crystallinity on the photocurrent response was also investigated by Zhang and Wang [67]. By using ITO glass covered with an electrodeposited Cu film as the substrate, they prepared $\text{Cu}_2\text{O}/\text{CuO}$ composites via galvanostatic anodization in 3 M NaOH for 30 min followed by calcination at $400 \text{ }^\circ\text{C}$ for 1 h. According to the authors, CuO is a very stable phase so it was used as a protection layer of the Cu_2O to prevent it from photocorrosion. Initially, the authors observed that the preferred orientations of the metallic Cu were affected by the applied potential in the electrodeposition step, which could influence the growth of the oxide in the following anodization step. The Cu_2O sample with (220) orientation exhibited a significantly better PEC performance than other samples, which the authors attributed to an electron mobility higher in (220) direction than in other directions. The authors

also observed that CuO nanostructure on top of Cu₂O inhibited both photocorrosion and recombination of electron and holes, increasing the overall PEC activity of the material.

Table 4. Photocathode architectures based on anodized copper oxides and maximum photocurrent densities obtained under experimental conditions indicated.

Photocathode	Method of Synthesis	Morphology	Maximum Photocurrent Density	LSV Experimental Condition	Irradiation Source	Ref.
CuO on Cu substrate ($E_g = 1.50$ eV)	Galvanostatic anodization, hydrothermal and annealing	Nanoneedles or nanoflakes	-4.6 mA cm ⁻² (at 0.05 V vs. RHE)	0.5 M Na ₂ SO ₄ , pH = 7 Range: 0.0 V to 0.8 V SR: 10 mV s ⁻¹	300 W XL with AM 1.5 G filter	[182]
Cu ₂ O@CuO on Cu substrate ($E_g = 2.01$ eV)	Galvanostatic anodization and annealing	Nanoflowers	-1.54 mA cm ⁻² (at -0.3 V vs. Ag AgCl)	0.5 M Na ₂ SO ₄ , pH = 6 Range: -0.5 V to 0.1 V	300 W XL with AM 1.5 G filter	[67]
Cu ₂ O on Cu substrate	Potentiostatic anodization	Sponge-like	-0.304 mA cm ⁻² (at -0.6 V vs. SHE)	0.5 M Na ₂ SO ₄ , pH = 9.6	35 W XL with a UV cut-off filter (100 mW cm ⁻²)	[175]
Cu ₂ O/CuO on Cu/ITO substrate	Galvanostatic anodization	Vertically aligned nanosheets	-1.54 mA cm ⁻² (at 0 V vs. NHE)	0.05 M Na ₂ SO ₅ , pH = 6.82 Range: 0.0 V to 0.6 V SR: 5 mV s ⁻¹	300 W XL with AM 1.5 G filter (100 mW cm ⁻²)	[31]
C-coated Cu ₂ O on Cu substrate ($E_g = 2.08$ eV)	Galvanostatic anodization and annealing	Nanowires with 200 nm diameter	-2.7 mA cm ⁻² (at 0 V vs. RHE)	0.5 M Na ₂ SO ₄ , pH = 6.23 Range: 0.0 V to 0.6 V SR: 5 mV s ⁻¹	300 W XL with AM 1.5 G filter (100 mW cm ⁻²)	[178]
AZO/TiO ₂ /RuO _x -covered Cu ₂ O/CuO on Cu/FTO substrate ($E_g \sim 2.0$ eV)	Galvanostatic anodization and annealing	Nanowire array with diameters 100–300 nm and lengths of 3–5 μ m	-10 mA cm ⁻² (at -0.3 V vs. RHE)	0.5 M Na ₂ SO ₄ + 0.1 M KH ₂ PO ₄ , pH = 5.0 Range: -0.3 V to 0.6 V SR: 10 mV s ⁻¹	450 W XL with AM 1.5 G filter (100 mW cm ⁻²)	[181]

SR—scan rate; XL—Xenon lamp.

A strategy to enhance simultaneously the efficiency and stability of a photocathode for water splitting was addressed by Shi et al. [178], which covered Cu₂O nanowires with a thin layer of carbon by immersion of the anodized oxide electrodes into glucose solution for 12 h followed by annealing at 550 °C in Ar atmosphere. For comparison, the authors prepared a sample without the glucose immersion step as reference. The authors observed that this procedure did not alter the morphology of the samples, however photocurrent density of the C-coated Cu₂O was significantly higher than that of the bare Cu₂O electrode. A maximum (IPCE) efficiency of 0.28% (at 0.21 V vs. RHE) was registered and it retained 61.3% of photoactivity after 1000 s of irradiation. Besides the photocurrent characterization, the authors also performed water-splitting experiments obtaining 6.64 μ mol of H₂ after passing 1.8 C (at 0 V vs. RHE) with a faradaic efficiency of 70%. According to the authors, the enhanced photostability indicated that the surface modification with carbon suppressed the redox activities of the Cu₂O nanowires photoelectrode and improved the photogenerated carrier separation and charge transfer.

In an insightful investigation, Luo et al. [181] explored both material properties as well as the PEC water-splitting application of a photocathode based on copper oxides. To fabricate a highly efficient and durable photocathode, the authors fabricated a Cu₂O/CuO heterostructure over a Cu thin film over FTO with a protective layer of Al-doped ZnO (AZO) and TiO₂ decorated with a RuO_x catalyst. Interestingly, they controlled the composition of the nanowire arrays only by the thickness

of the sputtered Cu film. To inhibit the contact of the exposed parts of the Cu metal substrate with the electrolyte, they passivate the exposed Cu before the deposition of the protective layer creating a blocking layer. From comparison with a similar but planar Cu₂O electrode, a significant enhancement of 25% in photo-response under sunlight-driven water-splitting was observed by using this novel architecture in the photocathode. IPCE spectra obtained under monochromatic illumination revealed an efficiency of ~75% in the 400–470 nm range, which decayed significantly with the increase of the wavelength, reaching values smaller than 20% in the 600–650 nm range. The authors observed a remarkable photocurrent response of 10 mA cm⁻² and stable operation up to 55 h, considered a new benchmark for copper oxides photocathodes.

These studies showed that morphology, crystallinity, and electronic properties are essential parameters affecting the performance of copper oxides photocathodes. Besides efficiency, the properties of the material must be designed taking into account its long-term stability and resistance to photocorrosion, which is still a major drawback for these semiconductors. In general, in the literature devoted to PEC water-splitting systems, since OER is the rate-limiting step [185], too much attention is given to the photoanodes in detrimental to photocathodes. These results showed the performance of a PEC device can be also strongly influenced by the photocathode. Low-costs, non-toxicity, and abundance of copper materials encourage further research in order to improve performance and economic competitiveness of the photocathode's fabrication.

8. Summary

The state-of-the-art review on the copper oxides reveal these materials can significantly contribute in numerous catalytic reactions bringing solutions in the emerging issues like greenhouse gases reduction or harvesting of clean energy. The major outcomes of the review can be listed in a few bullet points:

- Copper and copper-derived nanostructures display unique catalytic properties in electrochemical CO₂ reduction reaction: copper is the only pure metal that allows C₂₊ hydrocarbons and alcohols production; such catalysts possess moderately negative adsorption energy for *CO and slightly positive adsorption energy for *H—adsorption of *CO and consequently CO₂RR is preferred over HER.
- Oxide-derived copper catalysts possess superb affinity towards C₂₊ formation during CO₂RR, even when compared to bare copper; it prerequisites anodic copper oxides for applications in CO₂RR;
- Anodic copper oxides successfully contribute as catalysts in direct methanol fuel cells (DMFCs)—for these materials the highest value of turnover frequency (TOF) in methanol oxidation for non-precious metal was reported, reaching 3.5k s⁻¹ at the vortex potential of 0.65 V vs. Hg/HgO, OH⁻;
- Anodic copper oxides based glucose sensor achieve very high sensitivity due to their supreme electrocatalytic activity attributed to Cu(II)/Cu(III) redox couple, making the electrode highly sensitive and highly developed surface nanostructured materials;
- High surface area and band structure of the nanostructured anodic copper oxides contribute in photocatalytic degradation of water pollutants;
- Photoelectrochemical water splitting on the nanostructured anodic copper oxides has satisfactory performance due to the formed direct pathways for the photogenerated charge and highly-developed surface area; Cu₂O-CuO heterostructures provide rapid charge carrier separation, reducing the recombination of the photogenerated electrons.

Copper anodization is a controllable method for preparation of novel nanomaterials abundant with electronic and morphological features beneficial for photo- and electrochemistry. Its undoubtable application potential will ensure constant development of anodized copper electrodes. However, since anodization introduces multiple changes that may have impact on material properties,

an additional effort should be devoted to investigate and deeply understand structure-activity dependence in such systems. Narrowing the gap between computational and experimental approaches will bring mechanistic insight that will allow optimizing the anodization process for a specific application. By acquiring understanding on the role of material characteristics crucial for given surface current-assisted reaction it will be possible to design electrooxidation pre-treatment towards desired outcomes.

Anodized copper electrodes indicate exceptional performance in electrocatalysis. Nevertheless, their catalytic effectiveness can be tuned by cooperative influence from addition of second metal. Anodization of bimetallic systems seems to be one of the promising strategies for future development of photo- and electrocatalysis. Various metallic active sites within one material combined with highly-developed surface area rich with surface defects would provide new possibilities in designing highly efficient devices for e.g., CO₂ reduction, methanol oxidation, or water splitting. Due to its feasibility and controllability, anodization of copper and copper based bimetallic systems could be also employed for engineering of electrodes tailored for application in novel cell configurations, such as gas diffusion cells. In this matter, anodization step can be followed by further modification, including galvanic replacement or post-synthetic metal and metal oxides nanoparticles decoration, yielding new porous functional materials.

Author Contributions: Conceptualization, D.G., A.B. and W.J.S.; writing—original draft preparation, D.G., A.B., J.S.S. and W.J.S.; writing—review and editing, F.T.-S. and T.C.; visualization, D.G. and A.B.; supervision, W.J.S.; project administration, W.J.S. and D.G.; funding acquisition, W.J.S. and D.G. All authors have read and agreed to the published version of the manuscript.

Funding: This research was funded by Polish Returns 2019 Project granted from Polish National Agency for Academic Exchange (agreement no. PPN/PPO/2019/1/ 00003 /U/0001) and Polish National Science Center (NCN-MINIATURA4 DEC- 2020/04/X/ST5/00383). This publication was financially supported by statutory research funds of the Department of Functional Materials and Hydrogen Technology, Military University of Technology, Warsaw, Poland.

Conflicts of Interest: The authors declare no conflict of interest. The funders had no role in the design of the study; in the collection, analyses, or interpretation of data; in the writing of the manuscript, or in the decision to publish the results.

References

1. Abrahami, S.T.; Hauffman, T.; de Kok, J.M.M.; Terryn, H.; Mol, J.M.C. Adhesive bonding and corrosion performance investigated as a function of aluminum oxide chemistry and adhesives. *Corrosion* **2017**, *73*, 903–914. [[CrossRef](#)]
2. Suzuki, Y.; Kawahara, K.; Kikuchi, T.; Suzuki, R.O.; Natsui, S. Corrosion-resistant porous alumina formed via anodizing aluminum in etidronic acid and its pore-sealing behavior in boiling water. *J. Electrochem. Soc.* **2019**, *166*, C261–C269. [[CrossRef](#)]
3. González-Rovira, L.; González-Souto, L.; Astola, P.J.; Bravo-Benítez, C.; Botana, F.J. Assessment of the corrosion resistance of self-ordered anodic aluminum oxide (AAO) obtained in tartaric-sulfuric acid (TSA). *Surf. Coat. Technol.* **2020**, *399*, 126131. [[CrossRef](#)]
4. Masuda, H.; Fukuda, K. Ordered metal nanohole arrays made by a two-step replication of honeycomb structures of anodic alumina. *Science* **1995**, *268*, 1466–1468. [[CrossRef](#)]
5. Furneaux, R.C.; Rigby, W.R.; Davidson, A.P. The formation of controlled-porosity membranes from anodically oxidized aluminium. *Nature* **1989**, *337*, 147–149. [[CrossRef](#)]
6. Sousa, C.T.; Leitao, D.C.; Proenca, M.P.; Ventura, J.; Pereira, A.M.; Araujo, J.P. Nanoporous alumina as templates for multifunctional applications. *Appl. Phys. Rev.* **2014**, *1*, 031102. [[CrossRef](#)]
7. Nakajima, D.; Kikuchi, T.; Yoshioka, T.; Matsushima, H.; Ueda, M.; Suzuki, R.O.; Natsui, S.A. Superhydrophilic aluminum surface with fast water evaporation based on anodic alumina bundle structures via anodizing in pyrophosphoric acid. *Materials* **2019**, *12*, 3497. [[CrossRef](#)]
8. Norek, M.; Krasinski, A. Controlling of water wettability by structural and chemical modification of porous anodic alumina (PAA): Towards super-hydrophobic surfaces. *Surf. Coat. Technol.* **2015**, *276*, 464–470. [[CrossRef](#)]

9. Buijnsters, J.G.; Zhong, R.; Tsyntsar, N.; Celis, J.-P. Surface wettability of macroporous anodized aluminum oxide. *ACS Appl. Mater. Interfaces* **2013**, *5*, 3224–3233. [[CrossRef](#)]
10. Brudzisz, A.; Rajska, D.; Gajewska, M.; Sulka, G.D.; Brzózka, A. Controlled synthesis and characterization of AgPd nanowire arrays for electrocatalytic applications. *J. Electroanal. Chem.* **2020**, *873*, 114373. [[CrossRef](#)]
11. Date, M.K.; Yang, L.-H.; Yang, T.-Y.; Wang, K.-Y.; Su, T.-Y.; Wu, D.-C.; Cheuh, Y.-L. Three-dimensional CuO/TiO₂ hybrid nanorod arrays prepared by electrodeposition in AAO membranes as an excellent Fenton-like photocatalyst for dye degradation. *Nanoscale Res. Lett.* **2020**, *15*, 45. [[CrossRef](#)]
12. Wang, S.; Tian, Y.; Wang, C.; Hang, C.; Zhang, H.; Huang, Y.; Zheng, Z. One-step fabrication of copper nanopillar array-filled AAO films by pulse electrodeposition for anisotropic thermal conductive interconnectors. *ACS Omega* **2019**, *4*, 6092–6096. [[CrossRef](#)] [[PubMed](#)]
13. Salerno, M.; Reverberi, A.P.; Bairo, F. Nanoscale topographical characterization of orbital implant materials. *Materials* **2018**, *11*, 660. [[CrossRef](#)] [[PubMed](#)]
14. Toccafondi, C.; Dante, S.; Reverberi, A.P.; Salerno, M. Biomedical applications of anodic porous alumina. *Curr. Nanosci.* **2015**, *11*, 572–580. [[CrossRef](#)]
15. Bandyopadhyay, A.; Shivaram, A.; Mitra, I.; Bose, S. Electrically polarized TiO₂ nanotubes on Ti implants to enhance early-stage osseointegration. *Acta Biomater.* **2019**, *96*, 686–693. [[CrossRef](#)]
16. Maher, S.; Mazinani, A.; Barati, M.R.; Losic, D. Engineered titanium implants for localized drug delivery: Recent advances and perspectives of titania nanotubes arrays. *Expert Opin. Drug Deliv.* **2018**, *15*, 1021–1037. [[CrossRef](#)]
17. Bariana, M.; Kaidonis, J.A.; Losic, D.; Ranjitkar, S.; Anderson, P.J. Titania nanotube-based protein delivery system to inhibit cranial bone regeneration in Crouzon model of craniosynostosis. *Int. J. Nanomed.* **2019**, *14*, 6313–6324. [[CrossRef](#)]
18. Scisco, G.P.; Haynes, K.; Jones, K.S.; Ziegler, K.J. Single step bonding of thick anodized aluminum oxide templates to silicon wafers for enhanced system-on-a-chip performance. *J. Power Sources* **2020**, *474*, 228643. [[CrossRef](#)]
19. Acosta, L.K.; Bertó-Roselló, F.; Xifre-Perez, E.; Santos, A.; Ferré-Borrull, J.; Marsal, L.F. Stacked nanoporous anodic alumina gradient-index filters with tunable multispectral photonic stopbands as sensing platforms. *ACS Appl. Mater. Interfaces* **2019**, *11*, 3360–3371. [[CrossRef](#)]
20. Law, C.S.; Lim, S.Y.; Abell, A.D.; Voelcker, N.H.; Santos, A. Nanoporous anodic alumina photonic crystals for optical chemo- and biosensing: Fundamentals, advances, and perspectives. *Nanomaterials* **2019**, *8*, 788. [[CrossRef](#)]
21. Ashurov, M.; Gorelik, V.; Napolskii, K.; Klimonsky, S. Anodic alumina photonic crystals as refractive index sensors for controlling the composition of liquid mixtures. *Phot. Sens.* **2020**, *10*, 147–154. [[CrossRef](#)]
22. Wierzbicka, E.; Szultka-Młyńska, M.; Buszewski, B.; Sulka, G.D. Epinephrine sensing at nanostructured Au electrode and determination its oxidative metabolism. *Sens. Actuators B Chem.* **2016**, *237*, 206–215. [[CrossRef](#)]
23. Sadykov, A.I.; Kushnir, S.E.; Sapoletova, N.A.; Ivanov, V.K.; Napolskii, K.S. Anodic titania photonic crystals with high reflectance within photonic band gap via pore shape engineering. *Scripta. Mater.* **2020**, *178*, 13–17. [[CrossRef](#)]
24. Hu, H.; Xu, C.; Zhao, Y.; Ziegler, K.J.; Chung, J.N. Boiling and quenching heat transfer advancement by nanoscale surface modification. *Sci. Rep.* **2017**, *7*, 6117. [[CrossRef](#)]
25. Hu, H.; Xu, C.; Zhao, Y.; Shaeffer, R.; Ziegler, K.J.; Chung, J.N. Modification and enhancement of cryogenic quenching heat transfer by a nanoporous surface. *Int. J. Heat Mass Transf.* **2015**, *80*, 636–643. [[CrossRef](#)]
26. Wierzbicka, E.; Domaschke, M.; Denisov, N.; Fehn, D.; Hwang, I.; Kaufmann, M.; Kunstmann, B.; Schmidt, J.; Meyer, K.; Peukert, W.; et al. Magnéli phases doped with Pt for photocatalytic hydrogen evolution. *ACS Appl. Energy Mater.* **2019**, *2*, 8399–8404. [[CrossRef](#)]
27. Wierzbicka, E.; Zhou, X.; Denisov, N.; Yoo, J.; Fehn, D.; Liu, N.; Meyer, K.; Schmuki, P. Self-enhancing H₂ evolution from TiO₂ nanostructures under illumination. *ChemSusChem* **2019**, *12*, 1900–1905. [[CrossRef](#)]
28. Bashirov, N.; Tan, W.K.; Kawamura, G.; Matsuda, A.; Lockman, Z. Comparison of ZrO₂, TiO₂, and α-Fe₂O₃ nanotube arrays on Cr(VI) photoreduction fabricated by anodization of Zr, Ti, and Fe foils. *Mater. Res. Express* **2020**, *7*, 055013. [[CrossRef](#)]
29. Bashirov, N.; Razak, K.A.; Lockman, Z. Synthesis of freestanding amorphous ZrO₂ nanotubes by anodization and their application in photoreduction of Cr(VI) under visible light. *Surf. Coat. Technol.* **2017**, *320*, 371–376. [[CrossRef](#)]

30. Zhang, Z.; Zhong, C.; Liu, L.; Teng, X.; Wu, Y.; Hu, W. Electrochemically prepared cuprous oxide film for photo-catalytic oxygen evolution from water oxidation under visible light. *Sol. Energy Mater. Sol. Cells* **2015**, *132*, 275–281. [[CrossRef](#)]
31. Shu, X.; Zheng, H.; Xu, G.; Zhao, J.; Cui, L.; Qin, Y.; Wang, Y.; Zhang, Y.; Wu, Y. The anodization synthesis of copper oxide nanosheet arrays and their photoelectrochemical properties. *Appl. Surf. Sci.* **2017**, *412*, 505–516. [[CrossRef](#)]
32. Choi, Y.W.; Kim, S.; Seong, M.; Yoo, H.; Choi, J. NH₄-doped anodic WO₃ prepared through anodization and subsequent NH₄OH treatment for water splitting. *Appl. Surf. Sci.* **2015**, *324*, 414–418. [[CrossRef](#)]
33. Kikuchi, T.; Kawashima, J.; Natsui, S.; Suzuki, R.O. Fabrication of porous tungsten oxide via anodizing in an ammonium nitrate/ethylene glycol/water mixture for visible light-driven photocatalyst. *Appl. Surf. Sci.* **2017**, *422*, 130–137. [[CrossRef](#)]
34. Pisarek, M.; Krajczewski, J.; Wierzbicka, E.; Holdynski, M.; Sulka, G.D.; Nowakowski, R.; Kudelski, A.; Janik-Czachor, M. Influence of the silver deposition method on the activity of platforms for chemometric surface-enhanced Raman scattering measurements: Silver films on ZrO₂ nanopore arrays. *Spectrochim. Acta A Mol. Biomol. Spectrosc.* **2017**, *182*, 124–129. [[CrossRef](#)]
35. Ambroziak, R.; Hołdyński, M.; Płociński, T.; Pisarek, M.; Kudelski, A. Cubic silver nanoparticles fixed on TiO₂ nanotubes as simple and efficient substrates for surface enhanced Raman scattering. *Materials* **2019**, *12*, 3373. [[CrossRef](#)]
36. Celik, M.; Buyukserin, F. The use of anodized alumina molds for the fabrication of polymer nanopillar arrays as SERS substrates with tunable properties. *Vibrat. Spectrosc.* **2019**, *104*, 102965. [[CrossRef](#)]
37. Nyein, N.; Tan, W.K.; Kawamura, G.; Matsuda, A.; Lockman, Z. TiO₂ nanotube arrays formation in fluoride/ethylene glycol electrolyte containing LiOH or KOH as photoanode for dye-sensitized solar cell. *J. Photochem. Photobiol. A* **2017**, *343*, 33–39. [[CrossRef](#)]
38. Nyein, N.; Tan, W.K.; Kawamura, G.; Matsuda, A.; Lockman, Z. Anodic Ag/TiO₂ nanotube array formation in NaOH/fluoride/ethylene glycol electrolyte as a photoanode for dye-sensitized solar cells. *Nanotechnology* **2016**, *27*, 355605. [[CrossRef](#)]
39. Kikuchi, T.; Nishinaga, O.; Natsui, S.; Suzuki, R.O. Polymer nanoimprinting using an anodized aluminum mold for structural coloration. *Appl. Surf. Sci.* **2015**, *341*, 19–27. [[CrossRef](#)]
40. Pashchanka, M.; Yadav, S.; Cottre, T.; Schneider, J.J. Porous alumina-metallic Pt/Pd, Cr or Al layered nanocoatings with fully controlled variable interference colors. *Nanoscale* **2014**, *6*, 12877–12883. [[CrossRef](#)]
41. Tsuchiya, H.; Macak, J.M.; Sieber, I.; Schmuki, P. Self-organized high-aspect-ratio nanoporous zirconium oxides prepared by electrochemical anodization. *Small* **2005**, *1*, 722–725. [[CrossRef](#)] [[PubMed](#)]
42. Tsuchiya, H.; Macak, J.M.; Taveira, L.; Schmuki, P. Fabrication and characterization of smooth high aspect ratio zirconia nanotubes. *Chem. Phys. Lett.* **2005**, *410*, 188–191. [[CrossRef](#)]
43. Chilimoniuk, P.; Socha, R.P.; Czujko, T. Nanoporous anodic aluminum-iron oxide with a tunable band gap formed on the FeAl₃ intermetallic phase. *Materials* **2020**, *13*, 3471. [[CrossRef](#)]
44. Chilimoniuk, P.; Michalska-Domańska, M.; Czujko, T. Formation of nanoporous mixed aluminum-iron oxides by self-organized anodizing of FeAl₃ intermetallic alloy. *Materials* **2019**, *12*, 2299. [[CrossRef](#)] [[PubMed](#)]
45. Wong, M.H.; Berenov, A.; Qi, X.; Kappers, M.J.; Barber, Z.H.; Illy, B.; Lockman, Z.; Ryan, M.P.; MacManus-Driscoll, J.L. Electrochemical growth of ZnO nano-rods on polycrystalline Zn foil. *Nanotechnology* **2003**, *14*, 968–973. [[CrossRef](#)]
46. Stepniowski, W.J.; Misiolek, W.Z. Review of fabrication methods, physical properties, and applications of nanostructured copper oxides formed via electrochemical oxidation. *Nanomaterials* **2018**, *8*, 379. [[CrossRef](#)]
47. Beverskog, B.; Puigdomenech, I. Revised Pourbaix diagrams for copper at 25 to 300 °C. *J. Electrochem. Soc.* **1997**, *144*, 3476–3483. [[CrossRef](#)]
48. Stepniowski, W.J.; Yoo, H.; Choi, J.; Norek, M.; Józwick, P.; Misiolek, W.Z. Fabrication and characterization of oxide nano-needles formed by copper passivation in sodium hydroxide solution. *Thin Solid Films* **2019**, *671*, 111–119. [[CrossRef](#)]
49. Stepniowski, W.J.; Yoo, H.; Choi, J.; Chilimoniuk, P.; Karczewski, K.; Czujko, T. Investigation of oxide nanowires growth on copper via passivation in NaOH aqueous solution. *Surf. Interfaces* **2019**, *14*, 15–18. [[CrossRef](#)]

50. Stepniowski, W.J.; Stojadinovic, S.; Vasilic, R.; Tadic, N.; Karczewski, K.; Abrahamsi, S.T.; Buijnsters, J.G.; Mol, J.M.C. Morphology and photoluminescence of nanostructured oxides grown by copper passivation in aqueous potassium hydroxide solution. *Mater. Lett.* **2017**, *198*, 89–92. [[CrossRef](#)]
51. Xiao, F.; Yuan, S.; Liang, B.; Li, G.; Pehkonen, S.O.; Zhang, T.J. Superhydrophobic CuO nanoneedle-covered copper surfaces for anticorrosion. *J. Mater. Chem. A* **2015**, *3*, 4374–4388. [[CrossRef](#)]
52. Giri, S.D.; Sarkar, A. Electrochemical study of bulk and monolayer copper in alkaline solution. *J. Electrochem. Soc.* **2016**, *163*, H252–H259. [[CrossRef](#)]
53. Cheng, Z.; Ming, D.; Fu, K.; Zhang, N.; Sun, K. pH-controllable water permeation through a nanostructured copper mesh film. *ACS Appl. Mater. Interfaces* **2012**, *4*, 5826–5832. [[CrossRef](#)] [[PubMed](#)]
54. Wu, X.; Bai, H.; Zhang, J.; Chen, F.; Shi, G. Copper hydroxide nanoneedle and nanotube arrays fabricated by anodization of copper. *J. Phys. Chem. B* **2005**, *109*, 22836–22842. [[CrossRef](#)] [[PubMed](#)]
55. Wan, Y.; Zhang, Y.; Wang, X.; Wang, Q. Electrochemical formation and reduction of copper oxide nanostructures in alkaline media. *Electrochem. Commun.* **2013**, *36*, 99102. [[CrossRef](#)]
56. Allam, N.K.; Grimes, C.A. Electrochemical fabrication of complex copper oxide nanoarchitectures via copper anodization in aqueous and non-aqueous electrolytes. *Mater. Lett.* **2011**, *65*, 1949–1955. [[CrossRef](#)]
57. Jiang, W.; He, J.; Xiao, F.; Yuan, S.; Lu, H.; Liang, B. Preparation and antiscaling application of superhydrophobic anodized CuO nanowire surfaces. *Ind. Eng. Chem. Res.* **2015**, *54*, 6874–6883. [[CrossRef](#)]
58. Xie, J.F.; Huang, Y.X.; Li, W.W.; Song, X.N.; Xiong, L.; Yu, H.Q. Efficient electrochemical CO₂ reduction on a unique chrysanthemum-like Cu nanoflower electrode and direct observation of carbon deposit. *Electrochim. Acta* **2014**, *139*, 137144. [[CrossRef](#)]
59. Oyarzún Jerez, D.P.; López Tejjelo, M.; Ramos Cervantes, W.; Linarez Pérez, O.E.; Sánchez, J.; Pizarro, G.C.; Acosta, G.; Flores, M.; Arratia-Perez, R. Nanostructuring of anodic copper oxides in fluoride-containing ethylene glycol media. *J. Electroanal. Chem.* **2017**, *807*, 181186. [[CrossRef](#)]
60. Stepniowski, W.J.; Paliwoda, D.; Abrahamsi, S.T.; Michalska-Domanska, M.; Landskron, K.; Buijnsters, J.G.; Mol, J.M.C.; Terryn, H.; Misiolek, W.Z. Nanorods grown by copper anodizing in sodium carbonate. *J. Electroanal. Chem.* **2020**, *857*, 113628. [[CrossRef](#)]
61. Stepniowski, W.J.; Paliwoda, D.; Chen, Z.; Landskron, K.; Misiolek, W.Z. Hard anodization of copper in potassium carbonate aqueous solution. *Mater. Lett.* **2019**, *252*, 182–185. [[CrossRef](#)]
62. Stepniowski, W.J.; Misiolek, W.Z. Nanostructured anodic films grown on copper: A review of fabrication techniques and applications. In *Nanostructured Anodic Metals Oxides. Synthesis and Applications*, 1st ed.; Sulka, G.D., Ed.; Elsevier: Amsterdam, The Netherlands, 2020; pp. 415–452. [[CrossRef](#)]
63. Stepniowski, W.J.; Wang, K.-K.; Chandrasekar, S.; Paliwoda, D.; Nowak-Stepniowska, A.; Misiolek, W.Z. The impact of ethylenediaminetetraacetic acid (EDTA) additive on anodization of copper in KHCO₃-hindering Cu²⁺ re-deposition by EDTA influences morphology and composition of the nanostructures. *J. Electroanal. Chem.* **2020**, *871*, 114245. [[CrossRef](#)]
64. Le Coz, F.; Arurault, L.; Datas, L. Chemical analysis of a single basic cell of porous anodic aluminium oxide templates. *Mater. Character.* **2010**, *61*, 283–288. [[CrossRef](#)]
65. Takenaga, A.; Kikuchi, T.; Natsui, S.; Suzuki, R.O. Exploration for the self-ordering of porous alumina fabricated via anodizing in etidronic acid. *Electrochim. Acta* **2016**, *211*, 515–523. [[CrossRef](#)]
66. Wang, P.; Ng, Y.H.; Amal, R. Embedment of anodized p-type Cu₂O thin films with CuO nanowires for improvement in photoelectrochemical stability. *Nanoscale* **2013**, *5*, 2952–2958. [[CrossRef](#)] [[PubMed](#)]
67. Zhang, Z.; Wang, P. Highly stable copper oxide composite as an effective photocathode for water splitting via a facile electrochemical synthesis strategy. *J. Mater. Chem.* **2012**, *22*, 2456–2464. [[CrossRef](#)]
68. Arurault, L.; Belghith, M.H.; Bes, R.S. Manganese pigmented anodized copper as solar selective absorber. *J. Mater. Sci.* **2007**, *42*, 1190–1195. [[CrossRef](#)]
69. Mahmood, M.H.; Suryanto, S.; Al Hazza, M.H.F.; Haidera, F.I. Developing of corrosion resistance nano copper oxide coating on copper using anodization in oxalate solution. *Int. J. Eng. Trans. C* **2018**, *31*, 450–455.
70. Ratynski, M.; Hamankiewicz, B.; Krajewski, M.; Boczar, M.; Ziolkowska, D.; Czerwinski, A. Single step, electrochemical preparation of copper-based positive electrode for lithium primary cells. *Materials* **2018**, *11*, 2126. [[CrossRef](#)]
71. Wang, Z.; Zhang, Y.; Xiong, H.; Qin, C.; Zhao, W.; Liu, X. Yucca fern shaped CuO nanowires on Cu foam for remitting capacity fading of Li-ion battery anodes. *Sci. Rep.* **2018**, *8*, 6530. [[CrossRef](#)]

72. Qin, C.; Zhang, M.; Li, B.; Li, Y.; Wang, Z. Ag particles modified Cu_xO (x = 1, 2) nanowires on nanoporous Cu-Ag bimetal network for antibacterial applications. *Mater. Lett.* **2020**, *258*, 126823. [CrossRef]
73. Zoolfakar, A.S.; Rani, R.A.; Morfa, A.J.; O'Mullane, A.P.; Kalantar-zadeh, K. Nanostructured copper oxide semiconductors: A perspective on materials, synthesis methods and applications. *J. Mater. Chem. C* **2014**, *2*, 5247–5270. [CrossRef]
74. Pouloupoulos, P.; Baskoutas, S.; Pappas, S.D.; Garoufalis, C.S.; Droulias, S.A.; Zamani, A.; Kapaklis, V. Intense quantum confinement effects in Cu₂O thin films. *J. Phys. Chem. C* **2011**, *115*, 14839–14843. [CrossRef]
75. Goeppert, A.; Czaun, M.; Surya Prakash, G.K.; Olah, G.A. Air as the renewable carbon source of the future: An overview of CO₂ capture from the atmosphere. *Energy Environ. Sci.* **2012**, *5*, 7833. [CrossRef]
76. Earth System Research Laboratory. Global greenhouse gas reference network: Trends in atmospheric carbon dioxide. Available online: www.esrl.noaa.gov/gmd/ccgg/trends/mlo.html (accessed on 16 November 2020).
77. Intergovernmental Panel on Climate Change. *Climate Change 2014: Synthesis Report*; Intergovernmental Panel on Climate Change: Incheon, Korea, 2014.
78. Intergovernmental Panel on Climate Change. *IPCC Special Report on the Impacts of Global Warming of 1.5 °C-Summary for Policy Makers*; Intergovernmental Panel on Climate Change: Incheon, Korea, 2018.
79. Benson, E.E.; Kubiak, C.P.; Sathrum, A.J.; Smieja, J.M. Electrocatalytic and homogeneous approaches to conversion of CO₂ to liquid fuels. *Chem. Soc. Rev.* **2009**, *38*, 89. [CrossRef]
80. Montoya, J.H.; Shi, C.; Chan, K.; Nørskov, J.K. Theoretical insights into a CO dimerization mechanism in CO₂ electroreduction. *J. Phys. Chem. Lett.* **2015**, *6*, 2032–2037. [CrossRef]
81. Garza, A.J.; Bell, A.T.; Head-Gordon, M. Mechanism of CO₂ reduction at copper surfaces: Pathways to C₂ products. *ACS Catal.* **2018**, *8*, 1490–1499. [CrossRef]
82. Hori, Y.; Kikuchi, K.; Suzuki, S. Production of CO and CH₄ in electrochemical reduction of CO₂ at metal electrodes in aqueous hydrogencarbonate solutions. *Chem. Lett.* **1985**, *14*, 1695–1698. [CrossRef]
83. Hori, Y.; Kikuchi, K.; Murata, A.; Suzuki, S. Production of methane and ethylene in electrochemical reduction of carbon dioxide at copper electrode in aqueous hydrogencarbonate solution. *Chem. Lett.* **1986**, *15*, 897–898. [CrossRef]
84. Hori, Y.; Murata, A.; Takahashi, R.; Suzuki, S. Enhanced formation of ethylene and alcohols at ambient temperature and pressure in electrochemical reduction of carbon dioxide at a copper electrode. *J. Chem. Soc. Chem. Commun.* **1988**, *0*, 17. [CrossRef]
85. Bagger, A.; Ju, W.; Varela, A.S.; Strasser, P.; Rossmeisl, J. Electrochemical CO₂ reduction: A classification problem. *ChemPhysChem* **2017**, *18*, 3266–3327. [CrossRef] [PubMed]
86. Gameel, K.M.; Sharafaldin, I.M.; Abourayya, A.U.; Biby, A.H.; Allam, N.K. Unveiling CO adsorption on Cu surfaces: New insights from molecular orbital principles. *Phys. Chem. Chem. Phys.* **2018**, *20*, 25892–25900. [CrossRef] [PubMed]
87. Zhang, R.; Hao, X.; Duan, T.; Wang, B. Adsorption and activation of CO and H₂, the corresponding equilibrium phase diagrams under different temperature and partial pressures over Cu(100) surface: Insights into the effects of coverage and solvent effect. *Fuel Process. Technol.* **2017**, *156*, 253–264. [CrossRef]
88. Gao, D.; Arán-Ais, R.M.; Jeon, H.S.; Roldan Cuenya, B. Rational catalyst and electrolyte design for CO₂ electroreduction towards multicarbon products. *Nat. Catal.* **2019**, *2*, 198–210. [CrossRef]
89. Löffler, M.; Khanipour, P.; Kulyk, N.; Mayrhofer, K.J.J.; Katsounaros, I. Insights into liquid product formation during carbon dioxide reduction on copper and oxide-derived copper from quantitative real-time measurements. *ACS Catal.* **2020**, *10*, 6735–6740. [CrossRef]
90. Kibria, M.G.; Dinh, C.-T.; Seifitokaldani, A.; De Luna, P.; Burdyny, T.; Quintero-Bermudez, R.; Ross, M.B.; Bushuyev, O.S.; García de Arquer, F.P.; Yang, P.; et al. A surface reconstruction route to high productivity and selectivity in CO₂ electroreduction toward C₂+ hydrocarbons. *Adv. Mater.* **2018**, *30*, 1804867. [CrossRef]
91. Wan, Q.; Zhang, J.; Zhang, B.; Tan, D.; Yao, L.; Zheng, L.; Zhang, F.; Liu, L.; Cheng, X.; Han, B. Boron-doped CuO nanobundles for electroreduction of carbon dioxide to ethylene. *Green Chem.* **2020**, *22*, 2750–2754. [CrossRef]
92. Ting, L.R.; Pique, O.; Lim, S.Y.; Tanhaei, M.; Calle-Vallejo, F.; Yeo, B.S. Enhancing CO₂ electroreduction to ethanol on copper–silver composites by opening an alternative catalytic pathway. *ACS Catal.* **2020**, *10*, 4059–4069. [CrossRef]

93. Mandal, L.; Yang, K.R.; Motapothula, M.R.; Ren, D.; Lobaccaro, P.; Patra, A.; Sherburne, M.; Batista, V.S.; Yeo, B.S.; Ager, J.W.; et al. Investigating the role of copper oxide in electrochemical CO₂ reduction in real time. *ACS Appl. Mater. Interfaces* **2018**, *10*, 8574–8584. [[CrossRef](#)]
94. Zhang, F.; Chen, C.; Yan, S.; Zhong, J.; Zhang, B.; Cheng, Z. Cu@Bi nanocone induced efficient reduction of CO₂ to formate with high current densities. *Appl. Catal. A* **2020**, *598*, 117545. [[CrossRef](#)]
95. Jeon, H.S.; Kunze, S.; Scholten, F.; Cuenya, B.R. Prism-shaped Cu nanocatalysts for electrochemical CO₂ reduction to ethylene. *ACS Catal.* **2018**, *8*, 531–535. [[CrossRef](#)]
96. Jeong, H.M.; Kwon, Y.; Won, J.H.; Lum, Y.; Cheng, M.-J.; Kim, K.H.; Head-Gordon, M.; Kang, J.K. Atomic-scale spacing between copper facets for the electrochemical reduction of carbon dioxide. *Adv. Energy Mater.* **2020**, *10*, 1903423. [[CrossRef](#)]
97. Jimenez, C.; Cerrillo, M.I.; Martinez, F.; Camarillo, R.; Rincon, J. Effect of carbon support on the catalytic activity of copper-based catalyst in CO₂ electroreduction. *Sep. Purif. Technol.* **2020**, *248*, 117083. [[CrossRef](#)]
98. Gao, D.; McCrum, I.T.; Deo, S.; Choi, Y.-W.; Scholten, F.; Wan, W.; Chen, J.G.; Janik, M.J.; Cuenya, B.R. Activity and selectivity control in CO₂ electroreduction to multicarbon products over CuO_x catalysts via electrolyte design. *ACS Catal.* **2018**, *8*, 10012–10020. [[CrossRef](#)]
99. Wang, L. Electrochemical carbon monoxide reduction on polycrystalline copper: Effects of potential, pressure, and pH on selectivity toward multicarbon and oxygenated products. *ACS Catal.* **2018**, *8*, 7445–7454. [[CrossRef](#)]
100. Schlögl, R. Heterogeneous catalysis. *Angew. Chem. Int. Ed.* **2015**, *54*, 3465–3520. [[CrossRef](#)]
101. Verdager-Casadevall, A.; Li, C.W.; Johansson, T.P.; Scott, S.B.; McKeown, J.T.; Kumar, M.; Stephens, I.E.L.; Kanan, M.W.; Chorkendorff, I. Probing the active surface sites for CO reduction on oxide-derived copper electrocatalysts. *J. Am. Chem. Soc.* **2015**, *137*, 9808–9811. [[CrossRef](#)]
102. Gao, Y.; Wu, Q.; Liang, X.; Wang, Z.; Zheng, Z.; Wang, P.; Liu, Y.; Dai, Y.; Whangbo, M.-H.; Huang, B. Cu₂O nanoparticles with both {100} and {111} facets for enhancing the selectivity and activity of CO₂ electroreduction to ethylene. *Adv. Sci.* **2020**, *7*, 1902820. [[CrossRef](#)]
103. Zheng, Y.; Vasileff, A.; Zhou, X.; Jiao, Y.; Jaroniec, M.; Qiao, S.-Z. Understanding the roadmap for electrochemical reduction of CO₂ to multi-carbon oxygenates and hydrocarbons on copper-based catalysts. *J. Am. Chem. Soc.* **2019**, *141*, 7646–7659. [[CrossRef](#)]
104. Xiao, H.; Goddard, W.A.; Cheng, T.; Liu, Y. Cu metal embedded in oxidized matrix catalyst to promote CO₂ activation and CO dimerization for electrochemical reduction of CO₂. *Proc. Natl. Acad. Sci. USA* **2017**, *114*, 6685. [[CrossRef](#)]
105. Xiao, H.; Cheng, T.; Goddard, W.A. Atomistic mechanisms underlying selectivities in C1 and C2 products from electrochemical reduction of CO on Cu(111). *J. Am. Chem. Soc.* **2017**, *139*, 130–136. [[CrossRef](#)] [[PubMed](#)]
106. Lee, S.Y.; Jung, H.; Kim, N.-K.; Oh, H.-S.; Min, B.K.; Hwang, Y.J. Mixed copper states in anodized Cu electrocatalyst for stable and selective ethylene production from CO₂ reduction. *J. Am. Chem. Soc.* **2018**, *140*, 8681–8689. [[CrossRef](#)] [[PubMed](#)]
107. De Luna, P.; Quintero-Bermudez, R.; Dinh, C.-T.; Ross, M.B.; Bushuyev, O.S.; Todorovic, P.; Regier, T.; Kelley, S.O.; Yang, P.; Sargent, E.H. Catalyst electroreposition controls morphology and oxidation state for selective carbon dioxide reduction. *Nat. Catal.* **2018**, *1*, 103–110. [[CrossRef](#)]
108. Hori, Y.; Murata, A.; Takahashi, R. Formation of hydrocarbons in the electrochemical reduction of carbon dioxide at a copper electrode in aqueous solution. *J. Chem. Soc. Faraday Trans. 1* **1989**, *85*, 2309–2326. [[CrossRef](#)]
109. Varela, A.S.; Kroschel, M.; Reier, T.; Strasser, P. Controlling the selectivity of CO₂ electroreduction on copper: The effect of the electrolyte concentration and the importance of the local pH. *Catal. Today* **2016**, *260*, 8–13. [[CrossRef](#)]
110. Gupta, N.; Gattrell, M.; MacDougall, B. Calculation for the cathode surface concentrations in the electrochemical reduction of CO₂ in KHCO₃ solutions. *J. Appl. Electrochem.* **2006**, *36*, 161–172. [[CrossRef](#)]
111. Handoko, A.-D.; Ong, C.W.; Huang, Y.; Lee, Z.G.; Lin, L.; Panetti, G.B.; Yeo, B.S. Mechanistic insights into the selective electroreduction of carbon dioxide to ethylene on Cu₂O-derived copper catalysts. *J. Phys. Chem. C* **2016**, *120*, 20058–20067. [[CrossRef](#)]
112. Kortlever, R.; Shen, J.; Schouten, K.J.P.; Calle-Vallejo, F.; Koper, M.T. Catalysts and reaction pathways for the electrochemical reduction of carbon dioxide. *J. Phys. Chem. Lett.* **2015**, *6*, 4073–4082. [[CrossRef](#)]

113. Nie, X.; Esopi, M.R.; Janik, M.J.; Asthagiri, A. Selectivity of CO₂ reduction on copper electrodes: The role of the kinetics of elementary steps. *Angew. Chem. Int. Ed. Engl.* **2013**, *52*, 2459–2462. [[CrossRef](#)]
114. Ma, M.; Djanashvili, K.; Smith, W.A. Controllable hydrocarbon formation from the electrochemical reduction of CO₂ over Cu nanowire arrays. *Angew. Chem. Int. Ed.* **2016**, *55*, 6680–6684. [[CrossRef](#)]
115. Fields, M.; Hong, X.; Nørskov, J.K.; Chan, K. Role of subsurface oxygen on Cu surfaces for CO₂ electrochemical reduction. *J. Phys. Chem. C* **2018**, *122*, 16209–16215. [[CrossRef](#)]
116. Favaro, M.; Xiao, H.; Cheng, T.; Goddard, W.A.; Yano, J.; Crumlin, E.J. Subsurface oxide plays a critical role in CO₂ activation by Cu(111) surfaces to form chemisorbed CO₂, the first step in reduction of CO₂. *Proc. Natl. Acad. Sci. USA* **2017**, *114*, 6706. [[CrossRef](#)] [[PubMed](#)]
117. Eilert, A.; Cavalca, F.; Roberts, F.S.; Osterwalder, J.; Liu, C.; Favaro, M.; Crumlin, E.J.; Ogasawara, H.; Friebel, D.; Pettersson, L.G.M.; et al. Subsurface oxygen in oxide-derived copper electrocatalysts for carbon dioxide reduction. *J. Phys. Chem. Lett.* **2017**, *8*, 285–290. [[CrossRef](#)]
118. Wang, C.; Cao, M.; Jiang, X.; Wang, M.; Shen, Y. A catalyst based on copper-cadmium bimetal for electrochemical reduction of CO₂ to CO with high faradaic efficiency. *Electrochim. Acta* **2018**, *271*, 511–550. [[CrossRef](#)]
119. Lu, J.-J.; Jouny, M.; Luc, W.; Zhu, W.; Zhu, J.-J.; Jiao, F. A highly porous copper electrocatalyst for carbon dioxide reduction. *Adv. Mater.* **2018**, *30*, 1803111. [[CrossRef](#)]
120. Lu, L.; Sun, X.; Ma, J.; Yang, D.; Wu, H.; Zhang, B.; Zhang, J.; Han, B. Highly efficient electroreduction of CO₂ to methanol on palladium–copper bimetallic aerogels. *Angew. Chem. Int. Ed.* **2018**, *57*, 14149–14153. [[CrossRef](#)]
121. Hoang, T.T.H.; Verma, S.; Ma, S.; Fister, T.T.; Timoshenko, J.; Frenkel, A.J.; Kenis, P.A.J.; Gewirth, A.A. Nanoporous copper–silver alloys by additive-controlled electrodeposition for the selective electroreduction of CO₂ to ethylene and ethanol. *J. Am. Chem. Soc.* **2018**, *140*, 5791–5797. [[CrossRef](#)]
122. Deng, Y.; Huang, Y.; Ren, D.; Handoko, A.D.; Seh, Z.W.; Hirunsit, P.; Yeo, B.S. On the role of sulfur for the selective electrochemical reduction of CO₂ to formate on CuS_x catalysts. *ACS Appl. Mater. Interfaces* **2018**, *10*, 28572–28581. [[CrossRef](#)]
123. Li, C.W.; Kanan, M.W. CO₂ reduction at low overpotential on Cu electrodes resulting from the reduction of thick Cu₂O films. *J. Am. Chem. Soc.* **2012**, *134*, 7231–7234. [[CrossRef](#)]
124. Xu, Y.; Wang, H.; Yu, Y.; Tian, L.; Zhao, W.; Zhang, B. Cu₂O nanocrystals: Surfactant-free room-temperature morphology-modulated synthesis and shape-dependent heterogeneous organic catalytic activities. *J. Phys. Chem. C* **2011**, *115*, 31, 15288–15296. [[CrossRef](#)]
125. Kas, R.; Kortlever, R.; Milbrat, A.; Koper, M.T.M.; Mul, G.; Baltrusaitis, J. Electrochemical CO₂ reduction on Cu₂O-derived copper nanoparticles: Controlling the catalytic selectivity of hydrocarbons. *Phys. Chem. Chem. Phys.* **2014**, *16*, 12194–12201. [[CrossRef](#)] [[PubMed](#)]
126. Mistry, H.; Varela, A.S.; Bonifacio, C.S.; Zegkinoglou, I.; Sinev, I.; Choi, Y.; Kisslinger, K.; Stach, E.A.; Yang, J.C.; Strasser, P. Highly selective plasma-activated copper catalysts for carbon dioxide reduction to ethylene. *Nat. Commun.* **2016**, *7*, 1–8. [[CrossRef](#)] [[PubMed](#)]
127. Reller, C.; Krause, R.; Volkova, E.; Schmid, B.; Neubauer, S.; Rucki, A.; Schuster, M.; Schmid, G. Selective electroreduction of CO₂ toward ethylene on nano dendritic copper catalysts at high current density. *Adv. Energy Mater.* **2017**, *7*, 1602114. [[CrossRef](#)]
128. Li, J.; Kuang, Y.; Meng, Y.; Tian, X.; Hung, W.-H.; Zhang, X.; Li, A.; Xu, M.; Zhou, W.; Ku, H.-S.; et al. Electroreduction of CO₂ to formate on a copper-based electrocatalyst at high pressures with high energy conversion efficiency. *J. Am. Chem. Soc.* **2020**, *142*, 7276–7282. [[CrossRef](#)] [[PubMed](#)]
129. Akhade, S.A.; Luo, W.; Nie, X.; Bernstein, N.J.; Asthagiri, A.; Janik, M.J. Poisoning effect of adsorbed CO during CO₂ electroreduction on late transition metals. *Phys. Chem. Chem. Phys.* **2014**, *16*, 20429–20435. [[CrossRef](#)]
130. Lum, Y.; Yue, B.; Lobaccaro, P.; Bell, A.T.; Ager, J.W. Optimizing C–C coupling on oxide-derived copper catalysts for electrochemical CO₂ reduction. *J. Phys. Chem. C* **2017**, *121*, 14191–14203. [[CrossRef](#)]
131. Zhao, X.; Yin, M.; Ma, L.; Liang, L.; Liu, C.; Liao, J.; Lu, T.; Xing, W. Recent advances in catalysts for direct methanol fuel cells. *Eng. Environ. Sci.* **2011**, *4*, 2736–2753. [[CrossRef](#)]
132. Heli, H.; Jafarian, M.; Mahjani, M.G.; Gobal, F. Electro-oxidation of methanol in copper in alkaline solution. *Electrochim. Acta* **2004**, *49*, 4999–5006. [[CrossRef](#)]
133. Panah, N.B.; Danaee, I.; Ghamsari, Z.G. Effect of electrochemical surface pretreatment on electro-catalytic activity of copper for ethanol oxidation. *Surf. Eng. Appl. Electrochem.* **2019**, *55*, 630–637. [[CrossRef](#)]

134. Roy, A.; Jadhav, H.S.; Cho, M.; Seo, J.G. Electrochemical deposition of self-supported bifunctional copper oxide electrocatalyst for methanol oxidation and oxygen evolution reaction. *J. Ind. Eng. Chem.* **2019**, *76*, 515–523. [[CrossRef](#)]
135. Anantharaj, S.; Sugime, H.; Noda, S. Ultrafast growth of Cu(OH)₂-CuO nanoneedle array on Cu foil for methanol oxidation electrocatalysis. *ACS Appl. Mater. Interfaces* **2020**, *12*, 27327–27338. [[CrossRef](#)] [[PubMed](#)]
136. Pawar, S.M.; Pawar, B.S.; Inamdar, A.I.; Kim, J.; Jo, Y.; Cho, S.; Mali, S.S.; Hong, C.K.; Kwak, J.; Kim, H.; et al. In-situ synthesis of Cu(OH)₂ and CuO nanowire electrocatalysts for methanol electro-oxidation. *Matter. Lett.* **2017**, *187*, 60–63. [[CrossRef](#)]
137. Pawar, S.M.; Kim, J.; Inamdar, A.I.; Woo, H.; Jo, Y.; Pawar, B.S.; Cho, S.; Kim, H.; Im, H. Multi-functional reactively-sputtered copper oxide electrodes for supercapacitor and electro-catalyst in direct methanol fuel cell applications. *Sci. Rep.* **2016**, *6*, 21310. [[CrossRef](#)] [[PubMed](#)]
138. Zhong, H.; Wang, A.L.; Li, G.R.; Wang, J.W.; Ou, Y.N.; Tong, Y.X. Co₃O₄/Ni(OH)₂ composite mesoporous nanosheet networks as a promising electrode for supercapacitor applications. *J. Mater. Chem.* **2012**, *22*, 5656–5665. [[CrossRef](#)]
139. Xiong, X.; Ding, D.; Chen, D.; Waller, G.; Bu, Y.; Wang, Z.; Liu, M. Three-dimensional ultrathin Ni(OH)₂ nanosheets grown on nickel foam for high performance supercapacitors. *Nano Energy* **2015**, *11*, 154–161. [[CrossRef](#)]
140. El-Said, W.A.; AlMalki, W.A.; Sayed, E.M.; El-Hady, D.A.; Alshitari, W. Development of copper oxide nanostructures modified indium tin oxide electrode for electrochemical catalytically oxidation of methanol. *Mater. Lett.* **2020**, *279*, 128498. [[CrossRef](#)]
141. Xie, L.; Tang, C.; Wang, K.; Du, G.; Asiri, A.M.; Sun, X. Cu(OH)₂@CoCO₃(OH)₂·nH₂O core-shell heterostructure nanowire array: An efficient 3D anodic Catalyst for oxygen evolution and methanol electrooxidation. *Small* **2017**, *12*, 1602755. [[CrossRef](#)]
142. Torto, N.; Ruzgas, T.; Gorton, L. Electrochemical oxidation of mono- and disaccharides at fresh as well as oxidized copper electrodes in alkaline media. *J. Electroanal. Chem.* **1999**, *464*, 252–258. [[CrossRef](#)]
143. Li, Y.-L.; Kang, P.; Huang, H.-Q.; Liu, Z.-G.; Li, G.; Guo, Z. Porous CuO nanobelts assembly film for nonenzymatic electrochemical determination of glucose with high fabrication repeatability and sensing stability. *Sens. Actuat. B* **2020**, *307*, 127639. [[CrossRef](#)]
144. Meher, S.K.; Rao, G.R. Archetypal sandwich-structured CuO for high performance non-enzymatic sensing of glucose. *Nanoscale* **2013**, *5*, 2089. [[CrossRef](#)]
145. Ashok, A.; Kumar, A.; Tarlochan, F. Highly efficient nonenzymatic glucose sensors based on CuO nanoparticles. *Appl. Surf. Sci.* **2019**, *481*, 712–722. [[CrossRef](#)]
146. Liu, X.; Yang, W.; Chen, L.; Jia, J. Three-dimensional copper foam supported CuO nanowire arrays: An efficient non-enzymatic glucose sensor. *Electrochim. Acta* **2017**, *235*, 519–526. [[CrossRef](#)]
147. Li, C.; Su, Y.; Zhang, S.; Lv, X.; Xia, H.; Wang, Y. An improved sensitivity nonenzymatic glucose biosensor based on a Cu_xO modified electrode. *Biosens. Bioelectron.* **2010**, *26*, 903–907. [[CrossRef](#)] [[PubMed](#)]
148. Fan, H.-H.; Weng, W.-L.; Lee, C.-Y.; Liao, C.-N. Electrochemical cycling-induced spiky Cu_xO/Cu nanowire array for glucose sensing. *ACS Omega* **2019**, *4*, 12222–12229. [[CrossRef](#)]
149. Babu, T.G.S.; Ramachandran, T. Development of highly sensitive non-enzymatic sensor for the selective determination of glucose and fabrication of a working model. *Electrochim. Acta* **2010**, *55*, 1612–1618. [[CrossRef](#)]
150. Dat, P.V.; Viet, N.X. Facile synthesis of novel areca flower like Cu₂O nanowire on copper foil for a highly sensitive enzyme-free glucose sensor. *Mater. Sci. Eng. C* **2019**, *103*, 109758. [[CrossRef](#)] [[PubMed](#)]
151. Dhara, K.; Stanley, J.; Ramachandran, T.; Nair, B.G.; Babu, T.G.S. Cupric oxide modified screen printed electrode for the nonenzymatic glucose sensing. *J. Nanosci. Nanotech.* **2016**, *16*, 8772–8778. [[CrossRef](#)]
152. Li, X.; Wei, C.; Fu, J.; Wang, L.; Chen, S.; Li, P.; Li, H.; Song, Y. Electrolyte-controllable synthesis of Cu_xO with novel morphology and their application in glucose sensors. *RSC Adv.* **2014**, *4*, 52067. [[CrossRef](#)]
153. Lu, C.; Li, Z.; Ren, L.; Su, N.; Lu, D.; Liu, Z. In situ oxidation of Cu₂O crystal for electrochemical detection of glucose. *Sensors* **2019**, *19*, 2926. [[CrossRef](#)]
154. Wang, L.; Fu, J.; Hou, H.; Song, Y. A facile strategy to prepare Cu₂O/Cu electrode as a sensitive enzyme-free glucose sensor. *Int. J. Electrochem. Sci.* **2012**, *7*, 12587–12600.
155. Xu, L.; Yang, Q.; Liu, X.; Liu, J.; Sun, X. One-dimensional copper oxide nanotube arrays: Biosensors for glucose detection. *RSC Adv.* **2014**, *4*, 1449. [[CrossRef](#)]

156. Zhang, W.; Li, R.; Xing, L.; Wang, X.; Gou, X. Carnation-like CuO hierarchical nanostructures assembled by porous nanosheets for nonenzymatic glucose sensing. *Electroanalysis* **2016**, *28*, 2214–2221. [[CrossRef](#)]
157. Lin, L.-Y.; Karakocak, B.B.; Kavadiya, S.; Soundappan, T.; Biswas, P. A highly sensitive non-enzymatic glucose sensor based on Cu/Cu₂O/CuO ternary composite hollow spheres prepared in a furnace aerosol reactor. *Sens. Actuator. B* **2018**, *258*, 745–752. [[CrossRef](#)]
158. Jayasingha, L.; Jayathilaka, C.; Kumara, R.; Ohara, K.; Kaumal, M.; Guewardene, S.; Dissanayake, D.; Jayanetti, S. Nanoporous Cu₂O nanotube/nanorod array electrodes for non-enzymatic glucose sensing with high sensitivity and very low detection limit. *Electrochim. Acta* **2020**, *329*, 125177. [[CrossRef](#)]
159. Zhang, Q.; Li, M.; Wang, Z.; Qin, C.; Zhang, M.; Li, Y. Porous Cu_xO/Ag₂O (x = 1, 2) nanowires anodized on nanoporous Cu-Ag bimetal network as a self-supported flexible electrode for glucose sensing. *Appl. Surf. Sci.* **2020**, *515*, 146062. [[CrossRef](#)]
160. Zhang, Q.; Li, M.; Qin, C.; Wang, Z.; Zhao, W.; Li, Y. Flexible free-standing Cu_xO/Ag₂O (x = 1, 2) nanowires integrated with nanoporous Cu-Ag network composite for glucose sensing. *Nanomaterials* **2020**, *10*, 357. [[CrossRef](#)]
161. Wei, C.; Zou, X.; Liu, Q.; Li, S.; Kang, C.; Xiang, W. A highly sensitive non-enzymatic glucose sensor based on CuS nanosheets modified Cu₂O/CuO nanowire arrays. *Electrochim. Acta* **2020**, *334*, 135630. [[CrossRef](#)]
162. Marioli, J.M.; Kuwana, T. Electrochemical characterization of carbohydrate oxidation at copper electrodes. *Electrochim. Acta* **1992**, *37*, 1187. [[CrossRef](#)]
163. Wei, H.; Sun, J.-J.; Guo, L.; Li, X.; Chen, G.-N. Highly enhanced electrocatalytic oxidation of glucose and shikimic acid at a disposable electrically heated oxide covered copper electrode. *Chem. Commun.* **2009**, 2842. [[CrossRef](#)]
164. Luo, M.Z.; Baldwin, R.P. Characterization of carbohydrate oxidation at copper electrodes. *J. Electroanal. Chem.* **1995**, *387*, 87. [[CrossRef](#)]
165. Li, M.; Wang, Z.; Zhang, Q.; Qin, C.; Inoue, A.; Guo, W. Formation and evolution of ultrathin Cu₂O nanowires on NPC ribbon by anodizing for photocatalytic degradation. *Appl. Surf. Sci.* **2020**, *506*, 144816. [[CrossRef](#)]
166. Asahi, R.; Morikawa, T.; Ohwaki, T.; Aoki, K.; Taga, K. Visible-light photocatalysis in nitrogen-doped titanium oxides. *Science* **2001**, *293*, 269–271. [[CrossRef](#)] [[PubMed](#)]
167. Chakrabarti, S.; Dutta, B. Photocatalytic degradation of model textile dyes in wastewater using ZnO as semiconductor catalyst. *J. Hazard. Mater.* **2004**, *112*, 269–278. [[CrossRef](#)] [[PubMed](#)]
168. Vernardou, D.; Dorsos, H.; Fasoulas, J.; Koudoumas, E.; Katsarakis, N. Photocatalytic properties of chemically grown vanadium oxide at 65 °C. *Thin Solid Films* **2014**, *555*, 169–172. [[CrossRef](#)]
169. Zhou, T.W.; Zang, Z.G.; Wei, J.; Zheng, J.F.; Hao, J.Y.; Ling, F.L.; Tang, X.S.; Fang, L.; Zhou, M. Efficient charge carrier separation and excellent visible light photoresponse in Cu₂O nanowires. *Nano Energy* **2018**, *50*, 118–125. [[CrossRef](#)]
170. Yang, C.; Wang, J.; Mei, L.; Wang, X. Enhanced photocatalytic degradation of rhodamine B by Cu₂O coated silicon nanowire arrays in presence of H₂O₂. *J. Mater. Sci. Technol.* **2014**, *30*, 1124–1129. [[CrossRef](#)]
171. Li, M.; Li, Y.; Zhang, Q.; Qin, C.; Zhao, W.; Wang, Z.; Inoue, A. Ultrafine Cu₂O/CuO nanosheet arrays integrated with NPC/BMG composite rod for photocatalytic degradation. *Appl. Surf. Sci.* **2019**, *483*, 285–293. [[CrossRef](#)]
172. Zhang, Z.; Zhong, C.; Deng, Y.; Liu, L.; Wu, Y.; Hu, W. The manufacture of porous cuprous oxide film with photocatalytic properties via an electrochemical–chemical combination method. *RSC Adv.* **2013**, *3*, 6763. [[CrossRef](#)]
173. Kulkarni, S.K. *Nanotechnology: Principles and Practices*, 3rd ed.; Springer: New York, NY, USA, 2015; p. 418.
174. Grez, P.; Henríquez, R.; Muñoz, E.; Rojas, C.; Moreno, S.; Sessarego, G.; Heyser, C.; Celedón, C.; Schrebler, R. Sono-electrochemical synthesis of nanostructured of p-Cu₂O and n-Fe₂O₃ and their application for photoelectrochemical splitting of water. *Inter. J. Electrochem. Sci.* **2019**, *14*, 5646–5653. [[CrossRef](#)]
175. Mirzaei, M.; Soleymani, A.P.; Ashrafi, A.; Momeni, M.M. Electrochemically enhanced hydrothermal production of cupric oxide photoelectrode on copper substrate. *J. Electrochem. Soc.* **2020**, *167*, 066507. [[CrossRef](#)]
176. Jang, Y.J.; Lee, J.S. Photoelectrochemical water splitting with p-type metal oxide semiconductor photocathodes. *ChemSusChem* **2019**, *12*, 1835–1845. [[CrossRef](#)] [[PubMed](#)]
177. Dai, X.-C.; Hou, S.; Huang, M.-H.; Li, Y.-B.; Li, T.; Xiao, F.-X. Electrochemically anodized one-dimensional semiconductors: A fruitful platform for solar energy conversion. *J. Phys. Energy* **2019**, *1*, 022002. [[CrossRef](#)]

178. Shi, W.; Zhang, X.; Li, S.; Zhang, B.; Wang, M.; Shen, Y. Carbon coated Cu₂O nanowires for photo-electrochemical water splitting with enhanced activity. *Appl. Surf. Sci.* **2015**, *358*, 404–411. [[CrossRef](#)]
179. Zimbovskii, D.S.; Baranov, A.N. Synthesis of Cu₂O-based heterostructures and their photocatalytic properties for water splitting. *Inorg. Mater.* **2020**, *56*, 366–373. [[CrossRef](#)]
180. Li, R. Latest progress in hydrogen production from solar water splitting via photocatalysis, photoelectrochemical, and photovoltaic-photoelectrochemical solutions. *Chin. J. Catal.* **2017**, *38*, 5–12. [[CrossRef](#)]
181. Luo, J.; Steier, L.; Son, M.-K.; Schreier, M.; Mayer, M.T.; Grätzel, M. Cu₂O nanowire photocathodes for efficient and durable solar water splitting. *Nano Lett.* **2016**, *16*, 1848–1857. [[CrossRef](#)]
182. John, S.; Vadla, S.S.; Roy, S.C. High photoelectrochemical activity of CuO nanoflakes grown on Cu foil. *Electrochim. Acta* **2019**, *319*, 390–399. [[CrossRef](#)]
183. John, S.; Roy, S.C. CuO/Cu₂O nanoflake/nanowire heterostructure photocathode with enhanced surface area for photoelectrochemical solar energy conversion. *Appl. Surf. Sci.* **2020**, *509*, 144703. [[CrossRef](#)]
184. Qiu, Y.; Pan, Z.; Chen, H.; Ye, D.; Guo, L.; Fan, Z.; Yang, S. Current progress in developing metal oxide nanoarrays-based photoanodes for photoelectrochemical water splitting. *Sci. Bull.* **2019**, *64*, 1348–1380. [[CrossRef](#)]
185. Kang, J.S.; Kim, J.; Lee, M.J.; Son, Y.J.; Jeong, J.; Chung, D.Y.; Lim, A.; Choe, H.; Park, H.S.; Sung, Y.-E. Electrochemical synthesis of nanoporous tungsten carbide and its application as electrocatalysts for photoelectrochemical cells. *Nanoscale* **2017**, *9*, 5413–5424. [[CrossRef](#)]

Publisher’s Note: MDPI stays neutral with regard to jurisdictional claims in published maps and institutional affiliations.



© 2020 by the authors. Licensee MDPI, Basel, Switzerland. This article is an open access article distributed under the terms and conditions of the Creative Commons Attribution (CC BY) license (<http://creativecommons.org/licenses/by/4.0/>).